AGU PUBLICATIONS

JGR

Journal of Geophysical Research: Planets

RESEARCH ARTICLE
10.1002/2016JE005221

Key Points:
- Compositional buoyancy stabilizes melting-induced anomalies at the base of the lithosphere
- The anomalies may be detectable by gravimetry but not by seismics with a sparse station network
- Neglecting impact-induced mantle anomalies results in overestimation of the local crustal thickness

Supporting Information:
- Supporting Information S1
- Movie S1
- Movie S2

Correspondence to:
T. Ruedas,
t.ruedas@uni-muenster.de

Citation:
Ruedas, T. and D. Breuer (2017), On the relative importance of thermal and chemical buoyancy in regular and impact-induced melting in a Mars-like planet, *J. Geophys. Res. Planets*, *122*, 1554–1579, doi:10.1002/2016JE005221.

Received 14 NOV 2016
Accepted 2 JUL 2017
Accepted article online 7 JUL 2017
Published online 26 JUL 2017

On the relative importance of thermal and chemical buoyancy in regular and impact-induced melting in a Mars-like planet

Thomas Ruedas[1,2] **and Doris Breuer**[2]

[1]Institute of Planetology, Westfälische Wilhelms-Universität Münster, Münster, Germany, [2]Institute of Planetary Research, German Aerospace Center (DLR), Berlin, Germany

Abstract We ran several series of two-dimensional numerical mantle convection simulations representing in idealized form the thermochemical evolution of a Mars-like planet. In order to study the importance of compositional buoyancy of melting mantle, the models were set up in pairs of one including all thermal and compositional contributions to buoyancy and one accounting only for the thermal contributions. In several of the model pairs, single large impacts were introduced as causes of additional strong local anomalies, and their evolution in the framework of the convecting mantle was tracked. The models confirm that the additional buoyancy provided by the depletion of the mantle by regular melting can establish a global stable stratification of the convecting mantle and throttle crust production. Furthermore, the compositional buoyancy is essential in the stabilization and preservation of local compositional anomalies directly beneath the lithosphere and offers a possible explanation for the existence of distinct, long-lived reservoirs in the Martian mantle. The detection of such anomalies by geophysical means is probably difficult, however; they are expected to be detected by gravimetry rather than by seismic or heat flow measurements. The results further suggest that the crustal thickness can be locally overestimated by up to ∼20 km if impact-induced density anomalies in the mantle are neglected.

1. Introduction

In spite of the obvious and well-known geological evidence for their extent and ubiquity, the connection between meteorite impacts and the convective processes that shape the thermal and chemical evolution of planetary interiors still tends to be underappreciated. Among the first numerical studies of mantle convection that considered the effects of large impacts are those by *Reese et al.* [2002, 2004], which investigate how a basin-forming impact could introduce a strong thermal anomaly and trigger regional, potentially long-lived convection in a mantle that would otherwise convect only sluggishly. These authors already pointed to the potential of such an impact to seed a long-lived, stable superplume or other sort of thermal anomaly that feeds a major volcanic center, in their case the Tharsis province on Mars, as proposed earlier on the basis of geological evidence [e.g., *Schultz and Glicken*, 1979]. They also observed that impacts entail strong transient increases in melt production that result in the formation of thickened crust in the area affected by the impact and proposed that this may explain the areoid and topography of Tharsis.

Reese et al. [2002, 2004] started their simulations with the impact into a mantle in a simple, symmetric state assumed to represent preimpact conditions and described the heating and geometry of the impact as summarized by *Melosh* [1989]. In a more recent study, *Watters et al.* [2009] have refined the physical model of the impact, in particular with regard to the question how the depth-dependent properties of the target body affect shock propagation and, as a consequence, heating. They also account for the fact that the isobaric core of the impact lies at a certain depth below the preimpact surface. Their models demonstrate the dynamics of impact-induced plumes: while small events are obliterated quickly in the general flow of the mantle, large impacts cause a strong localized upwelling that results in a large anomaly that spreads beneath the lid and can sweep away cold downwellings. The upwelling induces a flow field that may attract plumes from its neighborhood and merges them, but on the other hand, the anomaly may reduce the convective vigor in the mantle as a whole. *Roberts and Arkani-Hamed* [2012] have extended this approach to the effects of multiple basin-forming impacts and also studied the effects of impact size and initial condition in some more detail.

Golabek et al. [2011] investigated the effects of an even larger, dichotomy-forming impact, but their focus lies more on core formation and the very earliest stages of Martian evolution.

Except for *Reese et al.* [2004] and *Golabek et al.* [2011], the previous workers did not consider compositional effects of impact-induced melting, and the paper by *Reese et al.* [2004] applies very simplistic models for both the impact, which is part of their initial condition, and the dependence of depletion and melt content on melting. On the other hand, various numerical convection studies of Martian mantle evolution did include compositional effects to some extent [e.g., *Schott et al.*, 2001; *Kiefer*, 2003; *Li and Kiefer*, 2007; *Keller and Tackley*, 2009; *Ogawa and Yanagisawa*, 2011, 2012; *Ruedas et al.*, 2013a, 2013b; *Plesa and Breuer*, 2014; *Breuer et al.*, 2016], but some of them do so only with regard to heat source concentrations, and none include impacts. In particular, *Schott et al.* [2001], *Ogawa and Yanagisawa* [2011, 2012], and *Plesa and Breuer* [2014] observed that the compositional density variations produced by melting may be crucial in establishing and preserving long-lived chemical heterogeneities in the Martian mantle; a similar observation was made by *Rolf et al.* [2017], who studied how basin-forming impacts may have altered lunar evolution. Furthermore, the review on the chemical reservoirs in the Martian interior by *Breuer et al.* [2016] includes some examples of simple local structures with anomalous density or viscosity and discusses their evolution, but these structures do not belong into any specific geological category.

In this study we consider both the thermal effects and the compositional changes from regular melting processes and in particular from melting induced by basin-forming impacts of different magnitudes, whereby the compositional changes are derived from a detailed mineralogical model. We compare the relative importance of the individual contributions of temperature and composition to buoyancy on the short-term as well as on the long-term evolution of a planet, which we assume to share many properties with Mars. In addition to the dynamical aspects, we also try to identify the effect of compositional variations on observables, in particular, density and seismic velocity.

2. Method

2.1. Convection and Mineral Physics Models

Our method builds upon or extends the approach described in detail in *Ruedas et al.* [2013a, 2013b], so we limit ourselves to a brief overview and describe shortly the more important changes and extensions. The convection code is a modified version of the code STAGYY [*Tackley*, 1996, 2008] and solves the equations of conservation of mass, momentum, and energy in the compressible, anelastic approximation on a two-dimensional spherical annulus grid [*Hernlund and Tackley*, 2008] with 512×128 points and stress-free, isothermal top and bottom boundaries. Melting and the transport of trace components such as water and radionuclides are modeled with tracer particles, with 50 tracers per cell. In impact sites as well as in any other partially molten region, we extract all melt down to the extraction threshold φ_r of 0.7% if the melt is less dense than the matrix and if there is a contiguous pathway of partially molten rock up to the base of the lithosphere. In terms of the redistribution of incompatible components, the use of such a threshold corresponds to the continuous or dynamic melting discussed in detail by *Shaw* [2000]. As in our previous work, all extracted melt is instantaneously added to the top to build the crust. Coupled to the convection model is a detailed model of the petrological properties of the mantle consisting of a parameterization of experimental phase diagrams of the Martian mantle, its melting behavior, and its thermoelastic properties such as the density, from which the buoyancy forces are derived. The thermoelastic properties are derived from the mineralogical model starting from mineral end-members and assuming ideal mixing; we replaced the polynomial-based parameterization of these properties from *Ruedas et al.* [2013b] with a formalism based on Mie–Grüneisen–Debye theory and used a database compiled from literature data from numerous experimental studies; a detailed description of several aspects of the mineralogical, rheological, and chemical model is given in the supporting information. Moreover, we have now also implemented a petrological model of basalt/eclogite and its properties at a similar level of detail as the peridotite. The calculation of thermal conductivities takes advantage of the new database by *Hofmeister and Branlund* [2015], which covers many of the relevant minerals, and applies effective medium theory to determine the bulk conductivity; compared with the former data set, it results in somewhat lower conductivities especially in the deeper parts of the mantle. The mineralogical model is also used for calculating melting partitioning coefficients, whereby we attempted to improve the previous work of *Ruedas et al.* [2013a, 2013b] by including dependence on pressure, temperature, and composition where applicable and possible. In particular, a better parameterization of iron partitioning is implemented for several mineral phases, which is an important factor in the relation between depletion and compositional buoyancy.

Moreover, the lattice strain model is applied to radionuclide partitioning in clinopyroxenes and garnets [e.g., *Wood and Blundy*, 2014]; a brief summary is given in the supporting information. The viscosity of the mantle depends on pressure, temperature, composition, and melt fraction as in the previous work (see supporting information). The density of the melt, which needs to be evaluated for several purposes, especially in order to determine whether it is extractable, is now calculated using the new deformable hard-sphere model from *Jing and Karato* [2011, 2012] rather than the less versatile model from *Jing and Karato* [2009] used in our previous work. As our petrological and melting model is not yet complete enough to yield the complete composition of the melt, we use the Martian crust major oxide composition from *Taylor and McLennan* [2009, Table 6.4] as input for the melt density model. Furthermore, we have revised our solidus parameterization using new data (see Appendix A).

The core enters the model as a thermal boundary condition on the interior boundary that represents the core–mantle boundary (CMB) and is described with an energy balance model following *Nimmo et al.* [2004] and *Williams and Nimmo* [2004] but with a more elaborate one-dimensional thermodynamical model of its properties that includes the calculation of adiabatic profiles of temperature and various physical properties for the core; the model is largely identical to that used in our previous work, with the difference that we now use material properties directly derived from experimental data not only for liquid iron, but also for liquid Fe-S alloys [*Kaiura and Toguri*, 1979; *Sanloup et al.*, 2000; *Balog et al.*, 2001, 2003; *Nishida et al.*, 2011].

2.2. Impact Shock Heating and Melt Production

The impact process is not included via coupling or interfacing the convection algorithm with a fully dynamical hydrocode simulation but is described using a combination of simpler analytical or semiempirical approximations. With regard to the energy input from the impact, we follow the approach pioneered by *Watters et al.* [2009] in many respects. When considering a large impact event such as the one that created Utopia, we start from the known diameter D_f of the final crater and use scaling laws for complex craters to work back to determine the diameter of the transient crater that is formed as an immediate consequence of the impact,

$$D_{tr} = \left(0.8547 D_f D_{s2c}^{0.13}\right)^{\frac{1}{1.13}} = 0.87028 D_f^{0.885} D_{s2c}^{0.115} \tag{1}$$

[*Melosh*, 2011], and of the impactor,

$$D_{imp} = 0.83 \left(\frac{\varrho}{\varrho_{imp}}\right)^{0.43} D_{tr}^{1.28} v_{z,imp}^{-0.56} g^{0.28} \tag{2}$$

[e.g., *Werner and Ivanov*, 2015]; the constant prefactor for the transient crater diameter accounts for the fact that the measured final (complex) crater diameter, which results from the collapse of the transient cavity, is measured from rim to rim rather than at the level of the reference surface and reduces it correspondingly [*Melosh*, 2011]. Here $v_{z,imp} = v_{imp} \sin \phi$ is the vertical component of the impactor velocity, D_{s2c} is the diameter of the transition between simple and complex craters, which is ~5.6 km (global mean from *Robbins and Hynek* [2012, Table 3]) for Mars, g is the acceleration of gravity, and ϱ and ϱ_{imp} are the densities of the target and the impactor, respectively; a list of the important symbols is given at the end of this paper. The impactor is assumed to be a rocky (S-type) asteroidal object hitting Mars with an absolute velocity of 9.6 km/s [*Ivanov*, 2001]. In the absence of more specific information, the angle ϕ is always set to 45°, which is the most probable impact angle for an isotropic impactor flux [e.g., *Gault and Wedekind*, 1978]. In the use of the scaling laws, we do not distinguish between complex craters and multiring basins, because it seems that the assumption of proportional growth is valid for the latter as well [*Spudis*, 1993], and numerical models indicate that many characteristics derived from scaling laws apply to large basins without modification [*Potter et al.*, 2015].

The most extreme conditions prevail in the central part of the impact region, which has been called "isobaric core" by some authors or "near field" by others and which is characterized by the near constancy of the pressure to which the shocked material is subjected. Many previous workers used empirical equations by *Pierazzo et al.* [1997] to determine the radius and depth of this region. We follow them in using their formula for the depth of its center below the surface (cf. Figure 1),

$$z_{ic} = 0.1525 D_{imp} v_{z,imp}^{0.361}, \tag{3}$$

but apply one of the new parameterizations of the recent low-v_{imp} data from *Monteux and Arkani-Hamed* [2016] by *Ruedas* [2017] to describe the dependence of shock pressure on distance, because the decay law

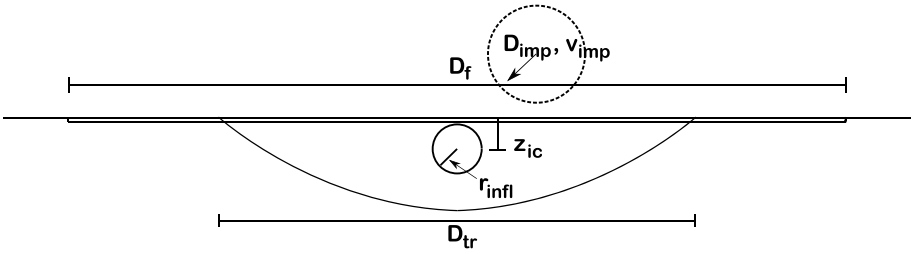

Figure 1. Key variables of the impact model. Final and transient crater depths are not to scale.

from *Pierazzo et al.* [1997] becomes increasingly erroneous at the low $v_{z,\mathrm{imp}}$ needed here. These parameterizations have the advantage of describing $p_s(r)$ accurately with a smooth function for all r and without imposing the impedance-match solution at $r = 0$. For an impact of a dunite meteorite onto a dunite target, the "inverse r" parameterization by *Ruedas* [2017] can be written in the form

$$p_s(r) = \frac{a}{b + \left(\frac{2r}{D_{\mathrm{imp}}}\right)^n} \tag{4}$$

with

$$a(v_{z,\mathrm{imp}}) = 0.081 p_{\mathrm{IM}} v_{z,\mathrm{imp}}^{1.478}, \tag{4a}$$

$$b(v_{z,\mathrm{imp}}) = 0.266 v_{z,\mathrm{imp}}^{1.161}, \tag{4b}$$

$$n(v_{z,\mathrm{imp}}) = -0.203 + 1.954 \lg v_{z,\mathrm{imp}} \tag{4c}$$

and $v_{z,\mathrm{imp}}$ in km/s. We caution that the coefficients for a, b, and n work reasonably well for the $v_{z,\mathrm{imp}}$ value of approximately 6.8 km/s assumed here but may not be suited for much higher $v_{z,\mathrm{imp}}$; the reader is referred to *Ruedas* [2017] for a detailed discussion.

Previous workers often also used the empirical definition by *Pierazzo et al.* [1997] for the radius of the isobaric core,

$$r_{\mathrm{PVM}} = 0.225 D_{\mathrm{imp}} v_{z,\mathrm{imp}}^{0.211}, \tag{5}$$

but as the models from which this formula was derived do not seem to cover the remote parts of the shocked regions for low v_{imp}, we suspect that the quality of equation (5) deteriorates in those cases. Therefore, we prefer to define the size of the isobaric core by the position of the inflection point of $p_s(r)$:

$$r_{\mathrm{infl}} = \frac{D_{\mathrm{imp}}}{2} \sqrt[n]{\frac{n-1}{n+1}} b. \tag{6}$$

The parameter p_{IM} is the impedance-match solution, which is used as a scaling factor and is calculated directly from the material properties using the Hugoniot equations as

$$p_{\mathrm{IM}} = \varrho (v_{\mathrm{B}} + S_{\mathrm{h}} u_{\mathrm{IM}}) u_{\mathrm{IM}}, \tag{7}$$

with the density of the target, ϱ, in g/cm^3, the speed of sound in the target, v_{B}, in km/s, and the Hugoniot slope $S_{\mathrm{h}} = (1 + \gamma)/2$ being related to the Grüneisen parameter γ [*Melosh*, 1989]. The particle velocity u_{IM} at the interface with the impactor is given by

$$u_{\mathrm{IM}} = \frac{-B_u + \sqrt{B_u^2 - 4 A_u C_u}}{2 A_u} \tag{8}$$

with

$$A_u = \varrho S_{\mathrm{h}} - \varrho_{\mathrm{imp}} S_{\mathrm{h,imp}} \tag{8a}$$

$$B_u = \varrho v_{\mathrm{B}} + \varrho_{\mathrm{imp}} (v_{\mathrm{B,imp}} + 2 S_{\mathrm{h,imp}} v_{z,\mathrm{imp}}) \tag{8b}$$

$$C_u = -\varrho_{\mathrm{imp}} v_{z,\mathrm{imp}} (v_{\mathrm{B,imp}} + S_{\mathrm{h,imp}} v_{z,\mathrm{imp}}) \tag{8c}$$

[e.g., *Melosh*, 2011]; the properties used here are those of the unshocked material, and the subscript "imp" indicates a property of the impactor. The speed of sound of the target is derived from the thermoelastic properties as given by the mineralogical model for the planet via $v_B = \sqrt{K_S/\varrho}$, where we use values for K_S and ϱ averaged over the isobaric core volume. The speed of sound in the impactor is simply determined using Birch's law, $v_{B,imp} = 2.36\varrho_{imp} - 1.75$ [e.g., *Poirier*, 2000], using an assumed density ϱ_{imp} of 2.7 g/cm^3 for mostly rocky (S-type) asteroidal impactors [e.g., *Fernández et al.*, 2015].

The propagation of the shock into the target and subsequent isentropic unloading put a certain amount of energy into the target and heat it. Reformulating an estimate by *Gault and Heitowit* [1963], *Watters et al.* [2009] write this impact heating in terms of shock pressure and lithostatic pressure p_l as

$$\Delta T = \frac{1}{c_p}\left[\frac{\Delta p}{2\varrho S_h}\left(1-\frac{1}{\Phi}\right) - \left(\frac{v_B}{S_h}\right)^2(\Phi - \ln\Phi - 1)\right] \tag{9}$$

with

$$\Phi = -\frac{2S_h\Delta p}{v_B^2\varrho}\left(1-\sqrt{\frac{4S_h\Delta p}{v_B^2\varrho}+1}\right)^{-1} \tag{9a}$$

$$\Delta p = p_s - p_l, \tag{9b}$$

where c_p is the specific heat capacity. The parameters ϱ, c_p, v_B, S_h, and p_l are derived directly from the convection and petrological model and are always positive; they are therefore functions of position, in particular of depth, which corresponds to the climbing shock model of *Watters et al.* [2009]. We note in passing that the form of equation (9) entails some limitations on p_s and p_l in order for ΔT to be finite, positive, and real. Inspection of the expressions indicates that this requires $\Phi > 0$ and that this condition is always met for $p_s > p_l$. For $p_s = p_l$, $\Phi = 1$ by de l'Hôpital's rule, and hence $\Delta T = 0$. For $p_s < p_l$, there are still real solutions as long as $p_l < p_s + v_B^2\varrho/(4S_h)$, but $\Delta T < 0$, and so we set the thermal perturbation to 0 as p_s drops below the lithospheric pressure.

In principle, melt production itself could be estimated from scaling laws [e.g., *Bjorkman and Holsapple*, 1987; *Pierazzo et al.*, 1997; *Abramov et al.*, 2012], but as this approach gives only bulk melt volumes but no information about the spatial distribution of the melt, it is not usually the approach taken in convection models. We consider directly where equation (9) leads to supersolidus temperatures and then calculate the amount of melt basically in the same manner as in regular melting processes. However, as the temperatures and melting degrees may be much higher in a giant impact, there will usually exist a region which is much more pervasively molten than normal melt-producing mantle, possibly beyond the rheological solid–liquid transition or even the liquidus. As convection in such a melt pond cannot be handled within the framework of a mantle convection code, we assume that the volume of the model shock-heated above the solidus melts according to the melting parameterization up to an imposed limit of 60% at which we assume that only a residue without any other fusible components would remain; the most extreme conditions are only reached at most in a small part of the shocked volume. The melt in excess of the extraction threshold φ_r is added to the top in the usual way as material that has cooled to surface temperature upon eruption. The source region is finally set to the temperature corresponding to φ_r, i.e., just above the solidus, for the aforementioned technical reasons; a similar numerical crutch for handling the high postimpact temperatures has also been used by previous workers [e.g., *Watters et al.*, 2009; *Roberts and Arkani-Hamed*, 2012]. Physically, this procedure can be justified by a combination of several processes: much of the waste heat corresponding to equation (9) is consumed by melting and vaporization; the postimpact melt pond is expected to cool much more rapidly thanks to its vigorous convection than the duration of a single time step of the mantle convection algorithm, which usually corresponds to at least several thousand to a few tens of thousands of years [e.g., *Reese and Solomatov*, 2006]; and a considerable fraction of the heat is extracted from the mantle along with the erupted melt and implicitly assumed to be lost to space as a consequence of our constant-T boundary condition.

2.3. Impact Crater and Ejecta Layer Formation

Prior to or simultaneously with causing these thermal effects at the impact site, the impact also forms a crater, a process that includes a modification of the local topography and the permanent redistribution of some of the material at the impact site. The transient crater created in the course of the impact is rapidly modified through slumping of the walls and similar processes in the case of larger events that form complex craters.

Although the fixed geometry of the numerical grid, the relatively coarse resolution of global models, and the complexity of ejecta ballistics prevent us from modeling these processes in any detail, we attempt to obtain an order-of-magnitude estimate of their basic features, because they potentially affect locally the thickness and composition of the crust, which in turn influences certain observables such as heat flow or gravity. We start by determining from which part of the transient crater material is ejected by calculating a number of mass parcel trajectories within the transient crater using the semianalytical Z model with a buried source [*Maxwell*, 1977; *Croft*, 1980; *Richardson et al.*, 2007]; material expelled by jetting during the first contact between impactor and target is not considered, as these jets seem to account for only a few percent of the total emitted material [*Johnson et al.*, 2014]. The transport of the ejecta outside the crater is approximated very simplistically in terms of ballistics of independent particles as suggested by *Tauber et al.* [1978], whereby the contributions of different particle sizes to the accumulated ejecta is given by empirical size–frequency distributions [*O'Keefe and Ahrens*, 1985, 1987]. The result of these calculations are estimates of the ejecta thickness as a function of distance from the impact site and of the ejected and displaced volumes; specifically, we can assess which part of the ejecta ends up within the boundaries of the future final crater. The collapse of the transient crater into the final crater cannot be modeled in any detail in our framework, and so we simply ignore the details of the final topography and impose that in the end the transient crater has transformed into a final crater with a level surface, in which slumped material from the transient crater walls and ejecta are all mixed into a uniform body, with the tracer particles being redistributed according to the final distribution of that material; the deposition of ejecta is treated as an influx of material with surface temperature. Each of these simple models is cheap enough in terms of computational effort to be included into the convection model as a subroutine. We note in passing that *Rolf et al.* [2017], who also gave consideration to the role of ejecta, describe ejecta blanket formation more straightforwardly in terms of empirical scaling laws but chose to assume zero thickness for ejecta inside the basin.

3. Results

3.1. Model Setup

In recent years, models of the Martian interior based on the analysis of geodetical and gravity data combined with petrological models have helped to tighten the constraints on the size of the Martian core. *Khan and Connolly* [2008] compiled some interior models, some of which featured a core size small enough to allow for a basal layer of perovskite (pv) and ferropericlase (fp) in the mantle. However, their own preferred model does not include such a layer, and the more recent investigations by *Konopliv et al.* [2011] and by *Rivoldini et al.* [2011] also point to a rather large core that would preclude the existence of a (pv + fp) layer; the latter study finds that such a layer would be marginally possible only in a hot mantle. Moreover, the impacts under consideration are not large enough to penetrate to depths that allow them to affect the core–mantle boundary region directly, so that the immediate dynamical effects would unfold in regions quite remote from a (pv + fp) layer. For these reasons, we decided to focus on models with a large core and no basal layer.

The chemical model assumed for the bulk mantle and crust is the one by *Wänke and Dreibus* [1994], although we do allow for some variability in the water content, having in mind that the water content of the Martian mantle is an unsettled issue and may be on the order of several hundred parts per million [e.g., *McCubbin et al.*, 2010, 2012], i.e., much higher than the 36 ppm suggested by *Wänke and Dreibus* [1994]. We assume this latter value in the major set of models, i.e., a fairly dry initial bulk silicate water content. In addition to these models, whose mantle quickly becomes almost dry, we also consider two further model series with initial bulk water contents of 72 and 144 ppm, i.e., 2 and 4 times the default value, respectively. This is enough to leave water contents at the tens-of-ppm level in the mantle, even though it lies lower than the values proposed for instance by *McCubbin et al.* [2012]; it may therefore correspond more closely to the scenarios suggested by *Wänke and Dreibus* [1994] or more recently by *McCubbin et al.* [2016] for the shergottite sources. At these concentrations, the effect of water on thermoelastic properties is not considered to be significant, and even the effect on the position of the solidus will be minor (although we do include it), but it is expected to lower the viscosity of the material noticeably, which is our main motivation for giving it consideration. For the core, we assume a sulfur content of 16 wt %, more similar to those favored by *Rivoldini et al.* [2011], i.e., slightly higher than *Wänke and Dreibus* [1994].

We assume an initial state prevailing at 4.4 Ga that is defined by mantle that is compositionally homogeneous and well mixed on large scales but is also already depleted by the production of the initial primordial crust; this state is implemented as a random pattern of low-degree depletion (~0.01 on average) throughout

Table 1. Model Parameters[a]

Parameters	Values
Planetary radius, R_P	3389.5 km
Total planetary mass, M	$6.4185 \cdot 10^{23}$ kg
Surface temperature	218 K
Mantle	
Mantle thickness, z_m	1659.5 km
Initial potential temperature, T_{pot}	1700 K
Initial core superheating	150 K
Surface porosity, φ_{surf}	0.2
Melt extraction threshold, φ_r	0.007
Bulk silicate Mars Mg#	0.75
Present-day K content	305 ppm
Present-day Th content	56 ppb
Present-day U content	16 ppb
Initial bulk water content	*36*, 72, 144 ppm
Core (Average Material Properties)	
Core radius	1730 km
Sulfur content	16 wt %
Thermal expansivity[b], α_c	$3.5–4.3 \cdot 10^{-5}$ 1/K
Isobaric specific heat, c_{pc}	750 J/(kg K)
Thermal conductivity[b], k_c	23.5–25.1 W/(m K)

[a]Default values of variable parameters are printed in italics.
[b]Varies with time.

the mantle that signifies that the entire mantle has experienced melting or has been mixed with residue from melting thoroughly in the transition from the magma ocean. The thickness of the resulting initial crust is not well constrained by observations but it is mostly dependent on the initial temperature.

As the objective of this study is the comparison of the contributions of thermally and compositionally induced density variations to the buoyancy, the models come in pairs that include one model each in which the compositional contribution to the buoyancy is suppressed by assigning the relevant physical properties of the unmolten material to the depleted material. In other words, in the "thermal-only" (T) model of each model pair, it is assumed that melting does not change the mineralogy and the iron content and hence also leaves density, thermal expansivity, etc. of the residue unchanged, whereas in the other model of the pair (TC), all these properties are functions of the melting degree f. However, we do treat the melting material in the T models as depleted residue in the usual sense as far as trace component partitioning or rheology are concerned, i.e., radionuclides and water are removed from the residue in all models.

The reference setup is a Mars-like planet with an initial potential mantle temperature T_{pot} of 1700 K, which is in the range deemed reasonable, e.g., with regard to the resulting crustal thickness, by previous studies [e.g., *Hauck and Phillips*, 2002; *Morschhauser et al.*, 2011] (Table 1). In most of the models with an impact, the reference model is struck by an S-type asteroid with a velocity of 9.6 km/s at an angle of 45° at 4 Ga, which corresponds to 400 Myr model evolution. The age of the impact is reasonably close (considering uncertainty) to the ages of three Martian craters of different size whose parameters we used to define the model impacts, namely, Utopia, Isidis, and Huygens (see Table 2); these three impacts are not intended to be faithful representations of the eponymous craters but serve as representatives covering a range of magnitudes that reaches from having a marginal effect on the mantle to the largest observed basin-forming event. Moreover, the planet has already evolved to some extent at this time and has formed a thermal lithosphere of a certain thickness; the most vigorous stage of regular melt production has already come to an end, so that the impact effects will stand out more clearly. Given crustal thicknesses around 79 km at the time of impact and a melt production zone for regular melting reaching down to $\gtrsim$330 km but reaching the strongest depletion at depths $\lesssim$200 km,

Table 2. Model Impacts[a]

Crater	D_f (km)	D_{imp} (km)	z_{ic} (km)	r_{PVM} (km)	r_{infl} (km)	Age (Ma)
Huygens	467.25	70.6	21.5	23.8	19.5	3980
Isidis	1352	243.5	74.1	81.9	67.1	3810–3960
Utopia	3380	699.2	212.9	235.2	192.6	3800–4111

[a]Final crater sizes are from the compilation by *Roberts et al.* [2009] after *Frey* [2008], ages are from the same source and from *Werner* [2008]. While we define the radius of the isobaric core according to equation (6), we also give the radius according to *Pierazzo et al.* [1997] (equation (5)) for reference.

Table 3. Model Pairs

Model Pair Name	Impact Size	C_{H_2O} (ppm)	Time of Impact
Ref-36	–	36	–
H-36	Huygens	36	400 Myr
I-36	Isidis	36	400 Myr
I-36m	Isidis	36	150 Myr
I-36e	Isidis	36	50 Myr
U-36	Utopia	36	400 Myr
U-36m	Utopia	36	150 Myr
U-36e	Utopia	36	50 Myr
Ref-72	–	72	–
I-72	Isidis	72	400 Myr
I-72m	Isidis	72	150 Myr
I-72e	Isidis	72	50 Myr
U-72	Utopia	72	400 Myr
U-72m	Utopia	72	150 Myr
U-72e	Utopia	72	50 Myr
Ref-144	–	144	–
I-144	Isidis	144	400 Myr
I-144e	Isidis	144	50 Myr
U-144	Utopia	144	400 Myr
U-144m	Utopia	144	150 Myr
U-144e	Utopia	144	50 Myr

these three impacts have the centers of their isobaric core toward the bottom of the main melting zone (Utopia), near its top (Isidis), and within the crust (Huygens). The isobaric cores correspondingly extend into the mantle below the melting zone in the case of Utopia, cover the crust and melting zone in the case of Isidis, and are limited to the crust in the case of Huygens, which should permit to reveal a possible effect of the relative positions of the preexisting regular global melting zone and the impact-generated anomaly. An effort was made to place the site of every impact so that it is located neither directly above a hot upwelling nor above major cold downwellings; as demonstrated by *Roberts and Arkani-Hamed* [2012], the preexisting convective features at the impact site can modify the effects of the impact, although its influence for instance on the impact-generated anomaly in the global heat flow does not exceed 10%. For this reason, the impacts appear at different positions in different models, as the different buoyancy mechanisms and water contents result in different convection patterns. An overview of all models is given in Table 3.

The timing of an impact is potentially important, especially in very young planets in which the lithospheric cooling rate is still high. In order to probe this dimension of parameter space, we ran two additional model series in which the impact occurred at 50 or 150 Myr model time; the uncertainties in crater statistics dating certainly warrant assuming different times. Because of the small effect of Huygens-sized events, we considered only Isidis- and Utopia-sized impacts in those cases. Apart from the timing, the model parameters are identical to the 400 Myr cases. Physically, the difference in the "earlier" cases is that the impactor meets a target that is already quite similar to that in the normal Isidis case as far as the extent and depletion of the regular melting zone and the thickness of the crust are concerned, but the thickness of thermal lithosphere is substantially smaller, such that the target volume is hotter on average.

3.2. Dynamical Evolution

The reference models start with a regular pattern of upwellings and downwellings that breaks down after a few tens of millions of years and transitions into a rather irregular flow; the impact of the "early" model pairs occur at a time when this transition begins. The Ref-36 models (see Table 3) slowly evolve from the chaotic stage toward the final convection pattern with five to seven stable plumes beginning after ~500 Myr, i.e., shortly after the time when the regular impacts would strike, whereas this final pattern begins to emerge several hundreds of millions of years later with increasing water content of the mantle.

In terms of the (effective) Rayleigh number $Ra_{\mathrm{eff}} = Ra_0/\eta_{\mathrm{mean}}$, the evolution of the reference models can be divided into two major phases (Figure 2): an early period of vigorous but declining convection that lasts until ~1.5 Gyr and a later period of nearly constant and calm flow that encompasses the remaining almost 3 Gyr. Irrespective of the water content, the T model variant generally convects a bit more energetically during the early stage, whereby the contrast with the TC variant is more pronounced in the model with low water content (36 ppm). The Ref-36 models convect at an approximately constant vigor during the first 1 Gyr, whereas the Ref-72 and Ref-144 models show a steep two-stage decline in their Rayleigh numbers, the first of which coincides essentially with the end of their principal period of crust formation. The mean mantle temperatures differ by less than ~10 K in most cases and decrease almost linearly throughout the evolution. Only the T variant of Ref-144 follows a somewhat different path, because the combination of the generally lower viscosity

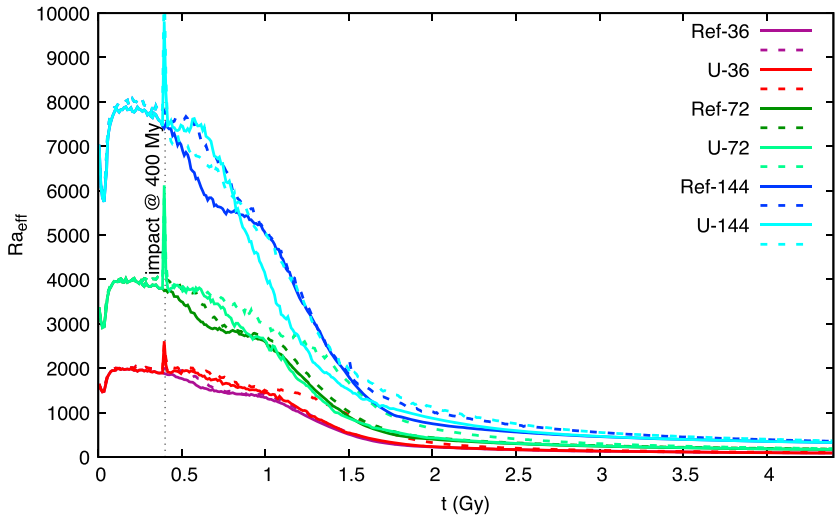

Figure 2. The 10 Myr averages of the effective Rayleigh number as a function of time for the reference models and the models with a Utopia-like impact at 400 Myr. Models with thermal and compositional buoyancy (TC) are plotted with solid lines and models with purely thermal buoyancy (T) with dashed lines.

and the relatively high density of the cooling uppermost mantle let it become gravitationally unstable and develop numerous downwellings, whereas its TC counterpart is stabilized by the additional compositional buoyancy in the melting zone.

An impact introduces an instantaneous local thermal disturbance that results in enhanced local heating and melting. This disturbance is visible as a spike signal in several parameters that characterize the thermal evolution, e.g., in the curves of Ra_{eff} in Figure 2, whereby the magnitude of the signal grows with increasing water content/decreasing viscosity, because a low-viscosity system reacts more strongly to any perturbation. In the models with an earlier impact, the evolution of Ra_{eff} is essentially the same, although in the 50 Myr series the spike of the impact is absorbed into the general initial steep increase of this parameter. As a consequence of the impact, a compositional anomaly characterized by enhanced depletion develops, as can be seen in the composition (f) images in Figure 3. The sequences in that figure and the corresponding animations in the supporting information show how the compositionally buoyant impact anomaly essentially stays in place for billions of years in the TC models, whereas it is dispersed within a few hundreds of millions of years in the T models. The density decrease due to heating and, in the TC models, due to the loss of higher-density constituents triggers a localized upwelling whose influence can reach far beyond the volume immediately affected by the impact itself. In the larger impacts, a hot pulse rapidly spreads out beneath the lithosphere and reinforces melting and crust formation if the center of the isobaric core lies deep enough. In a very large impact, the upwelling modifies the flow field on a regional scale such that preexisting plumes may be drawn toward the impact site and merge. In most models with larger impacts, this effect persists for several hundreds of millions of years, i.e., much longer than the actual lifetime of the thermal anomaly of a few tens of millions of years, suggesting that a very large (Utopia-sized) impact can enforce a fairly stable regional flow field that is self-sustaining to some extent under favorable conditions; the TC model from U-36 establishes such a long-lived plume for billions of years, as can be seen in Figure 4 (top row). In a more vigorous convective regime as in its wetter counterparts from U-72 and U-144, the enhanced stirring disturbs the stability of the structure and shortens its lifetime the more the higher the water content is, although the direct hot-material surge from the impact spreads further due to the lower viscosity. In the model series with earlier impacts, there is a tendency of globally reinforced crust production and delamination, but the effect is insignificant except for the 144 ppm water model of the Utopia-sized event, in which a substantial amount of crustal material is reintroduced into the mantle. In the corresponding T models, the local effect decays much faster, on timescales of severals tens rather than hundreds of millions of years because of the absence of the self-stabilizing compositional anomaly, although the general reinvigoration of convection tends to be a bit more persistent than in the TC models, judging from Figure 2. Figure 4 (bottom left) shows that there is no plume near the former impact site 2 Gyr after the impact, although the convection pattern is nonetheless not as regular as that of the reference model shown in Figure 4 (bottom right). This underscores that the compositional buoyancy

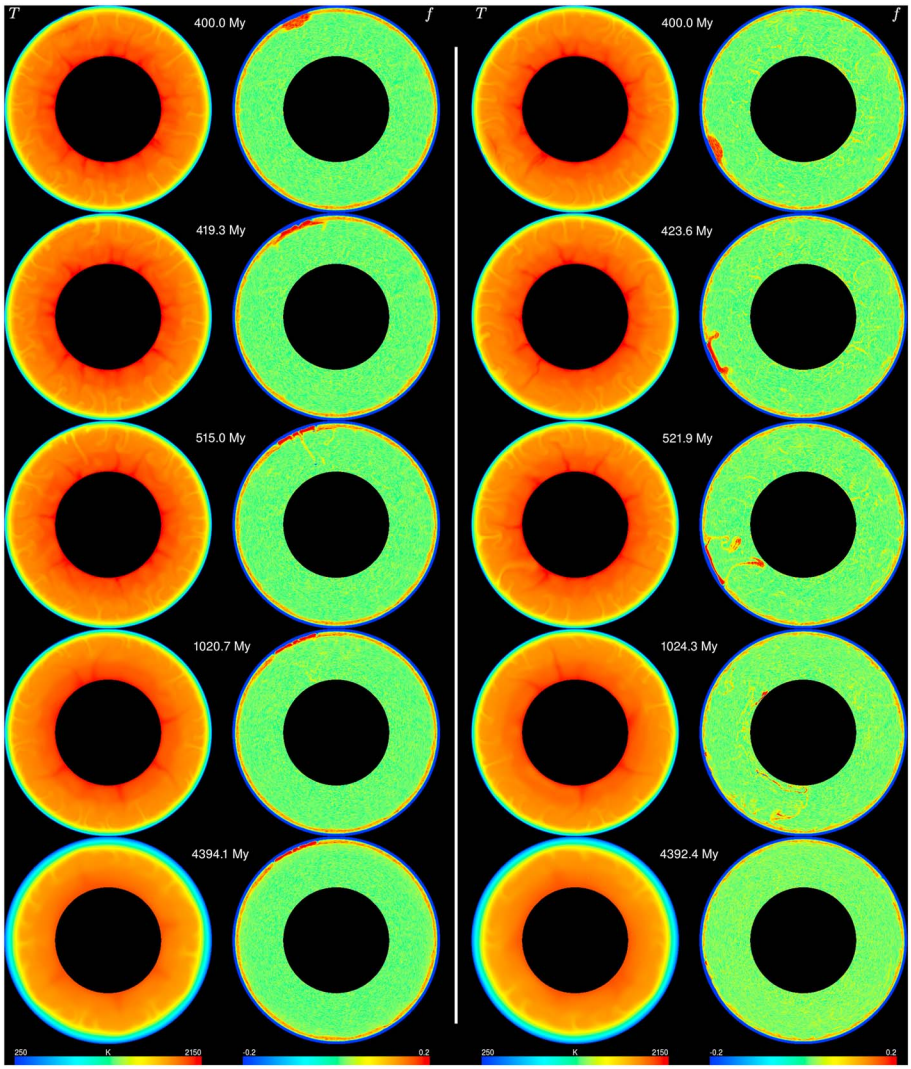

Figure 3. Evolution of temperature and composition in the model pair I-36. (left) Model with thermal and compositional buoyancy; (right) model with purely thermal buoyancy. In the images of composition, a positive melting degree *f* indicates depleted material; the crust is displayed as strongly "enriched" (dark blue). The color bars are clipped for clarity. Animations of the evolution of both models are available online as supporting information.

of the impact-induced anomaly must contribute significantly to the establishment of the stable flow field. An effect is also well visible in the TC models of Isidis-sized impacts, but it is less long-lived and extensive, whereas it is insignificant in the T versions. In the Huygens-sized events (H-36), which are essentially confined to the thermal lithosphere, there is no effect beyond a small, short-lived local disturbance.

A large part of the crust—approximately 59 km—is produced in the initialization step as "primordial" crust, and crustal growth is strongest at the beginning and declines toward 0 afterward. In the reference models the crust usually reaches its final thickness after 1–1.5 Gyr, reaching values higher by a few kilometers in models with higher mantle water contents. The amount of crust added after initialization lies between approximately 20 and 25 km in most cases; only the T variants of the models with 144 ppm water experience more voluminous and protracted crust formation thanks to the reinforcement of convection by the cold downwellings. In some regions that have been fed by plumes over extended periods, the crust eventually grows thick enough to delaminate; nonetheless, delamination is generally not a quantitatively important process, and the small amount of delaminated material is mixed into the deeper mantle within a few tens of millions of years. In Ref-144/T and its impact-affected derivatives delamination is more extensive, because the downwellings drag not only lithospheric mantle but also a part of the thick crust with them, but it does nonetheless not reach a global scale that affects the entire crust.

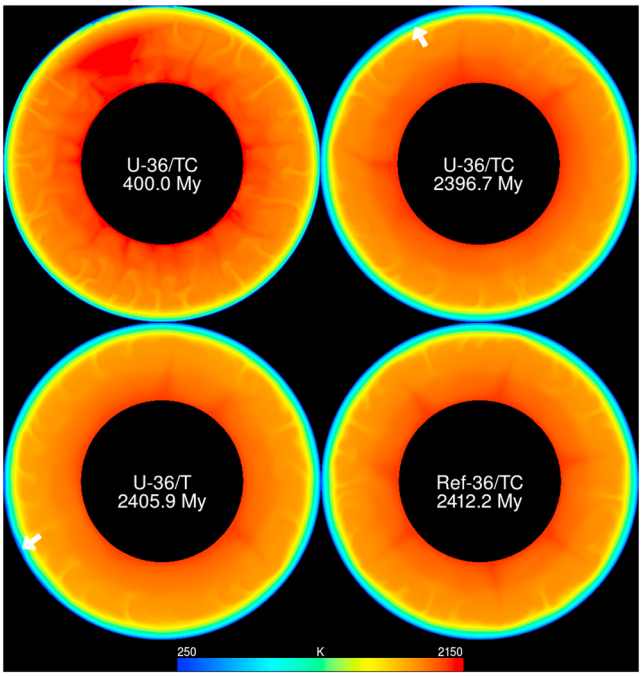

Figure 4. Temperature field of the TC model from U-36 at the time of the impact, and temperature fields of models U-36 (TC), U-36 (T), and Ref-36 (TC) about 2 Gyr later. The white arrows mark the impact sites. The color bar is clipped for clarity.

The enhanced melting and crust formation at an impact site may also result in a thicker crust, but on the other hand, the removal of crustal material by crater formation may compensate to some extent the growth of the crust. In all models, we find that the T variant develops a thicker postimpact crust at the impact site than its TC counterpart, because the buoyant residue from the impact was less stable and hence less efficient at preventing the ascent of fertile material into the melting zone. The postimpact thickening is largely due to the immediate melt production from the impact in the TC models and therefore finishes within a few tens of millions of years, whereas in the T models, the enhanced crustal formation persists for hundreds of millions of years. The extent to which the crust grows depends on the water content of the mantle and the time of the impact: early impacts and/or higher water contents generally entail a thicker crust, because the lower viscosity allows the mantle to convect more vigorously and produce more melt. In the two larger sorts of impact, the postimpact crust is always thicker than the mean of the reference model due to the additional melt production, whereas the Huygens-sized events do not produce enough melt to compensate the removal of crust by the impact itself. Crustal thickness variations exist directly after the impact, but they tend to flatten out soon by spreading laterally as a consequence of the buoyancy forces of the crust and the underlying mantle anomaly, as well as the action of shear forces from divergent mantle flow at its base. Postimpact melt production and crust formation are facilitated by thermal "rejuvenation" of the lithosphere caused by the impact, which produces a local pit-like low-viscosity zone with a lifetime of several tens of millions of years in the boundary region between crust and mantle. An example for this phenomenon is visible at the impact sites of the I-36 models in Figure 3. This process seems to be more efficient in the T models, where the root is less protected by a stable density anomaly in the underlying mantle. Figure 5 summarizes the principal stages of the postimpact evolution after a large basin-forming impact.

3.3. Observables

A variety of geophysical and geochemical observables can be derived from the models. Although it is not our primary goal to reproduce in detail observations from Mars, we will draw comparisons with results from missions to that planet in the following and concentrate on some observables for which data are relatively abundant or which are expected to become available in the near future as results from the InSight mission.

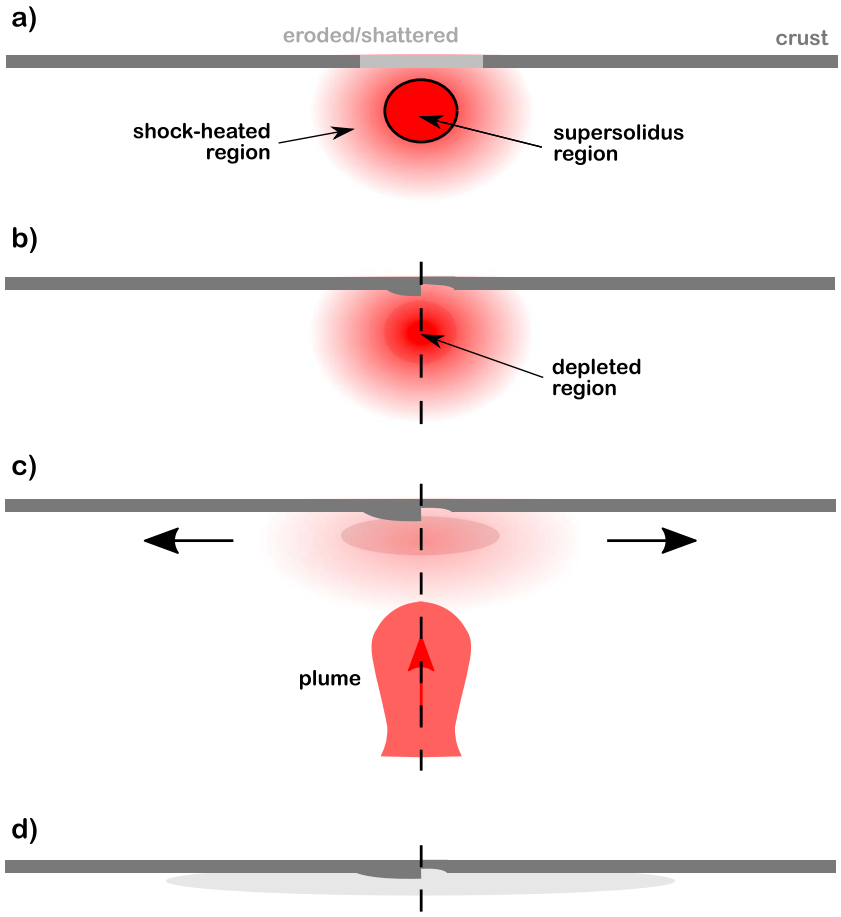

Figure 5. Postimpact evolution of a thermochemical anomaly generated by a basin-forming impact. (a) Shortly after the impact, the crust around the impact site is removed or shattered, and a large region around the center of the isobaric core is shock-heated, partly to temperatures above the solidus. (b) The melt extracted from the supersolidus region leaves behind a depleted residue in the mantle and has formed a new crust together with preimpact crustal material from the final crater. In the left part of this and the following stages, the new crust is thicker than average, in the right part it is thinner; which variant develops in any given crater depends on the magnitude of the impact and the amount of melt produced by it. (c) The thermochemical anomaly rises due to its buoyancy and may trigger a plume from the CMB or attract one from nearby. With time the thermal component of the anomaly fades, whereas the compositional is not much diminished. The rising plume may produce additional crust. (d) Final stage: the thermal anomaly and the plume have disappeared, whereas the compositional anomaly has spread out at the base of the lithosphere/crust and remains in place. Variations in the thickness of the crust may be leveled to some extent by creep. The figures are not to scale.

3.3.1. Surface Heat Flow, q_s, and Elastic Thickness of the Lithosphere, z_{el}

The heat flux estimates from spacecraft missions have so far usually been derived from flexure or admittance models and are mean heat flows through the elastic lithosphere; comparable fluxes from numerical models could be derived using the temperature difference between the top and bottom of the elastic lithosphere, its thickness, and its average thermal conductivity, as done by *Ruedas et al.* [2013a, 2013b]. The HP^3 experiment on the InSight mission, by contrast, is a real heat flux probe designed to determine the actual surface heat flux at the landing site; this is not identical to the mean lithospheric heat flow, but it can be approximated in a numerical model by a finite-difference formulation using the outermost grid cell layer. In this study, we consider the surface heat flow and the elastic thickness of the lithosphere, which is determined as an intermediate step in the calculation of the mean lithospheric heat flow and should be more readily comparable to independent data as it requires fewer assumptions.

The determination of the elastic thickness of the lithosphere from flexure models usually involves the use of non-Newtonian rheology, which is not part of our numerical model. A direct comparison is therefore not possible, but one can still attempt an estimate by assuming an average lithospheric strain rate $\dot{\epsilon}$ and a yield stress σ_y

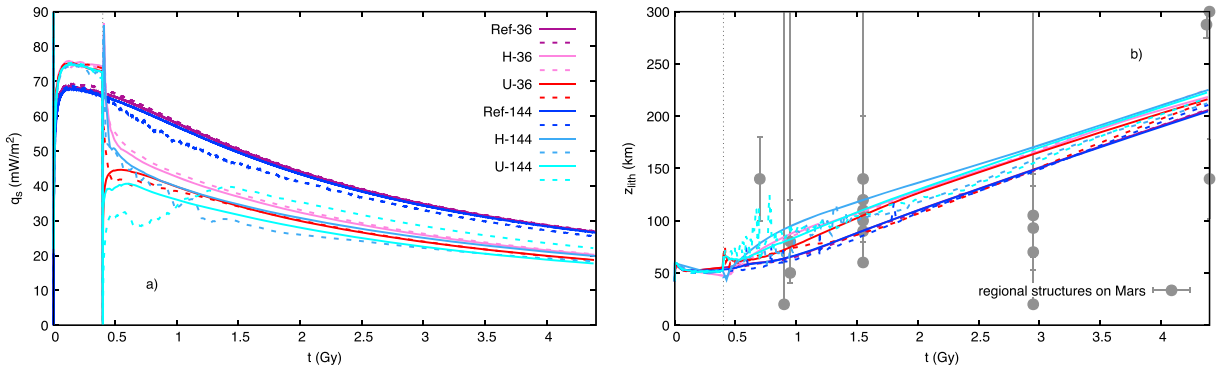

Figure 6. (a) Surface heat flow and (b) elastic thickness of the lithosphere of selected models as a function of time; the curves for the reference models are global means, the curves for the models with impacts show the average within the final crater. TC models are plotted with solid lines, T models with dashed lines. Observation-based elastic thickness values are for regional structures [*McGovern et al.*, 2004; *Barnett and Nimmo*, 2002; *Belleguic et al.*, 2005; *Phillips et al.*, 2008; *Wieczorek*, 2008; *Ritzer and Hauck*, 2009]. The ages are averages, in most cases based on the age estimates of the corresponding era, and will usually have uncertainties on the order of hundreds of millions of years.

typical for lithospheric materials. We follow *Grott and Breuer* [2008], who assumed a strain rate of 10^{-17} s^{-1} and yield stress of 15 MPa and then solve the Arrhenius-type flow law for non-Newtonian creep for temperature:

$$T_{bd} = \frac{Q}{R_{gas}} \left[\ln \left(\frac{B \sigma_y^{\nu}}{\dot{\epsilon}} \right) \right]^{-1}, \tag{10}$$

where the factor B, the activation enthalpy Q, and the exponent ν are 3.1×10^{-20} Pa$^{-3.05}$s^{-1}, 276 kJ/mol, and 3.05 for wet crustal diabase and 2.4×10^{-16} Pa$^{-3.5}$s^{-1}, 540 kJ/mol, and 3.5 for dry mantle olivine, respectively; in this context, "wet" means that the material is saturated with water, which is already the case for the volumetrically (and thus rheologically) important minerals at very low concentrations under the low pressure conditions of the crust. We allow for the possibility of an incompetent layer separating the crust and mantle segments of the elastic lithosphere but did not actually observe such a configuration in our models. Therefore, the elastic thickness of the lithosphere is tied to a single temperature T_{bd} as defined in equation (10). Associated with the brittle–ductile transition of the mantle (~1065 K in our case), similar to *Ruedas et al.* [2013a, 2013b], whose transition temperature was a few dozen kelvins lower; the depth at which this temperature is reached is taken to represent z_{el}. In some instances, structures like cold downwellings make it difficult to determine reasonably the local elastic thickness, and it seems safer to discard such regions when computing the global mean; this problem arose in the models with low water content especially in the time interval from ~250 Myr to ~1.5 Gyr, and therefore the corresponding curves in Figure 6b should be regarded as approximate only in that time interval.

The surface heat flow of the reference models (Figure 6) shows a small increase at the earliest stage of evolution before declining smoothly toward present-day values close to 26.5 mW/m^2; the curves are almost the same in all reference models except for that initial phase (Figure 6a). In general, the heat flux does not show large variation in the reference models: deviations from the global mean by more than 1–2 mW/m^2 are rare. The elastic thicknesses grow almost linearly for most of the time toward a modern value of a bit more than 200 km, except for some minor variability during the first few hundreds of millions of years; the elastic thicknesses in the Ref-144 pair are some 20 km larger than those of the Ref-36 pair, but the difference decreases as the planet evolves. All models are broadly consistent with most literature data, especially for the first 1.5 Gyr (Figure 6b); in such comparisons it must be kept in mind that several of the heat flow estimates were made for specific regional structures such as volcanic edifices or graben and that their age is very uncertain.

Impact events produce a sudden change in the conditions near the surface in the surroundings of the impact site: they shock-heat the interior beneath the point of impact and trigger melt production, which leads to magmatic activity. In our treatment, we assume that (1) the erupted material loses heat quickly and can therefore be set to surface temperature and that (2) a large volume of ejecta is produced, much of which is deposited as a layer of several kilometers thickness and with surface temperature within the crater. The surface porosity within the crater is assumed to be 0 due to melt filling the voids. The heat flux in the affected area, i.e., within the final crater, is strongly reduced but returns to higher levels with time, although the levels

of undisturbed areas are not reached again; only in the case of the Huygens-sized events is the drop preceded by a spike-like maximum, which in that case is due to the direct heating effect of the impact itself. The temporal heat flux evolutions for any given impact size are quite similar for all three impact times in terms of the amplitude of the disturbance and the duration of its decay and result in almost identical regional present-day heat flows. Moreover, the regional heat flux evolutions of the Isidis-size and the Utopia-sized events at 400 Myr are very similar at any given water content, such that the curves for the Utopia-sized models in Figure 6a are fairly representative for both. The reason for the reduction of the heat flow, which is contrary to intuition and to the findings of other authors [e.g., *Roberts and Arkani-Hamed*, 2012], is that these large events produce a substantial amount of ejecta and erupted material that is assumed to have surface temperature when being deposited as a layer, whose ejecta component alone can be more than 10 km thick. This material is represented as a cold influx that shifts isotherms downward and thus causes a very shallow temperature gradient that reduces the heat flow, especially inside the final crater. This effect of ejecta and other shattered material was not taken into consideration in most previous studies. *Rolf et al.* [2017] do not observe the cooling effect in their models of the Moon, because they treat ejecta deposition in a different way and assume that ejecta are absent within the basin; they find a reduced heat flux just beyond the final crater rim, which in their case is due to the reduced thermal conductivity of the relatively thick ejecta deposits there. Moreover, the crust formed in the crater in our models is produced from high-degree melting of a source that was already partly depleted, so that its content in heat-producing elements is several times lower than the average, resulting in a reduced crustal contribution to the surface heat flux. The hot pulse from the mantle diffuses only slowly upward and is then consumed in heating the cool ejecta-thickened crust. The present-day elastic thickness of the lithosphere beneath the crater in models with impacts is usually not significantly different from the global mean of impact-free models, reaching values between 200 and ~230 km, irrespective of the time of impact; the only stronger deviation from this pattern is the U-144 model pair for an impact at 50 Myr model time, in which z_{el} reaches values around 250 km.

On a global scale, even large impacts produce only a small instantaneous negative excursion from the values of the reference models, followed by an exponential-like return toward the heat flux of the corresponding reference model within a few tens of millions of years. The thermal disturbance from a single impact early in the planet's history decays quickly on the timescale of planetary evolution and leaves no distinguishable trace today. In this context it is worth pointing out that a calculation of global mean values by computing the surface heat flow for every single grid column, summing, and dividing by the number of columns as done for the reference models would be misleading in two-dimensional models with impacts and is therefore omitted here. The reason is that a single local anomaly like an impact site occupies a certain fraction of the domain that is larger than the true fraction of the entire planet that is affected by an impact in three dimensions, because the two-dimensional geometry implicitly extends that anomaly along half a meridian in the third dimension, making its spatial extent potentially much larger than it would be in three dimensions. As a consequence, it contributes more to the mean than it would in three dimensions, thus resulting in an overestimate. Although this applies, in principle, to all major intrinsically three-dimensional structures in two-dimensional models, the effects of structures that are ubiquitous in the model and can make positive or negative contributions to the mean may cancel out reasonably well for the purpose of calculations such as mean global heat flow estimates; this is unfortunately not the case with a single local structure such as an impact. Appendix B gives a simple estimate of this geometrical error and indicates that the true amplitudes of the impact signal would be 1 to 2 orders of magnitude smaller even for large impacts.

3.3.2. Density and Seismic Velocities

Our thermoelastic properties model directly yields the density ϱ of the crust and mantle at different depletions. Subtraction of the laterally averaged density-depth profiles of the T model from the TC model of a model pair indicates that the compositional density difference due to melting is up to 30 kg/m^3; locally, as in impact-generated anomalies with very high depletion, it may exceed 50 kg/m^3. This additional contribution to buoyancy has certain dynamical implications that become especially important on a local scale in the models with impacts, as can be seen by comparing the evolutions of the two models of a given pair. In impacts that are large enough to reach into the mantle, the anomaly created by the strong heating and depletion has a large buoyancy and rises toward the base of the lithosphere, where it tends to spread, as mentioned above (cf. Figure 3). Contrary to the thermal anomaly, which vanishes as the excess heat diffuses away, the depletion anomaly could only be destroyed by remixing. This does indeed happen in the T models, but the compositional contribution to the buoyancy active in the TC models helps to stabilize the anomaly in those cases. The signature of the impact is clearly visible in present-day depth profiles of depletion of the TC models at the site,

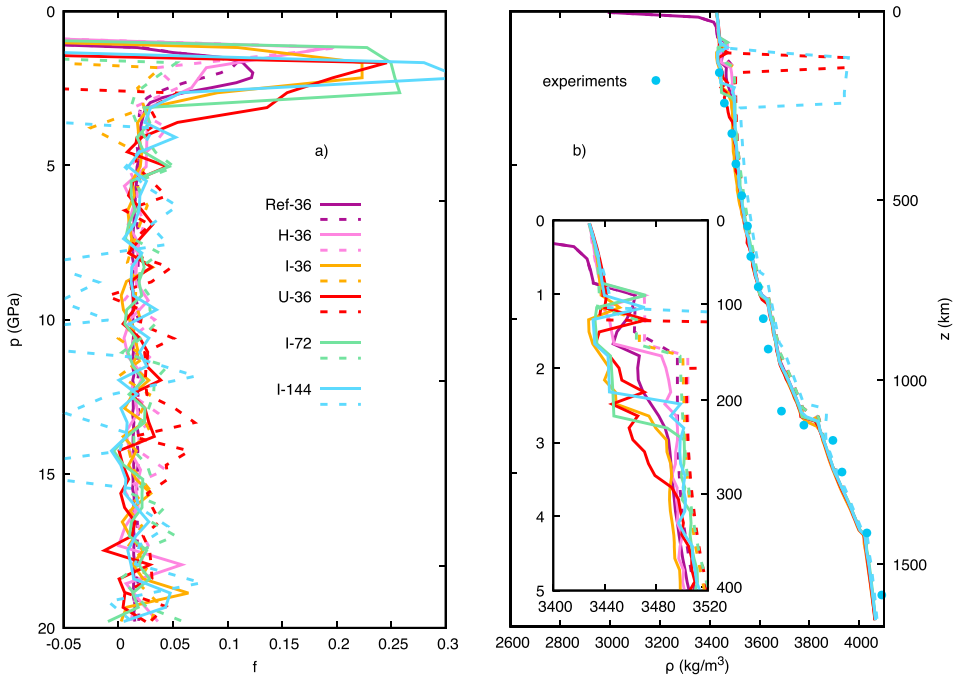

Figure 7. Mantle depth (pressure) profiles of (a) depletion and (b) density at 4.4 Gyr for selected models. The profiles of the reference models are laterally averaged profiles, the profiles of the models with impacts were taken at the impact site; the depletion profiles of the latter set were smoothed for clarity. Also shown are experimentally determined densities from *Bertka and Fei* [1998] for a composition modeled after *Wänke and Dreibus* [1994].

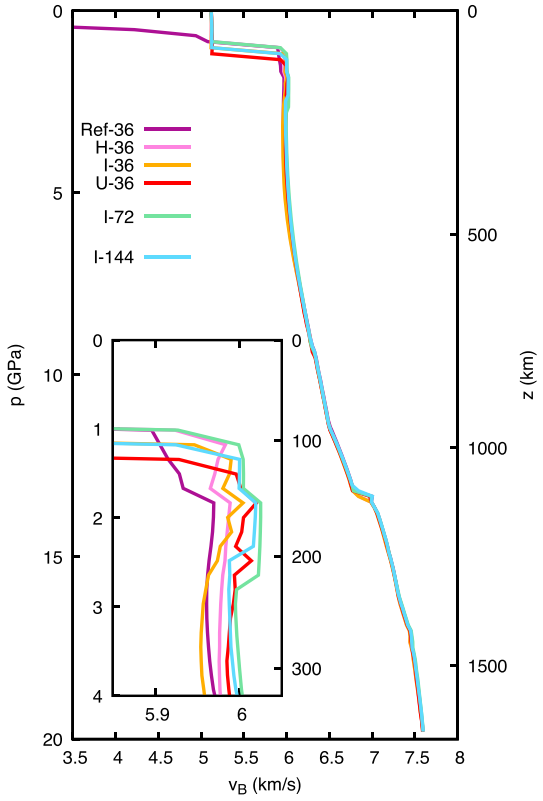

Figure 8. Mantle depth (pressure) profile of bulk sound velocity from TC models from the 36 ppm water series at 4.4 Gyr. The Ref-36 profile is laterally averaged; the profiles of the models with impacts were taken at the impact site.

where the preserved depletion from the event is still nearly up to 3 times as high as the average maximum of impact-free models. It is correlated with density anomalies (Figure 7b), i.e., it has survived 4 Gyr of planetary evolution, whereas it has largely vanished in the T models. The inset figure, which covers the uppermost 400 km/5 GPa of the mantle, shows clearly the density deficit of the compositional anomalies of the two larger impact categories relative to the reference model, whereas the uppermost slice of mantle below the Huygens site happens to be less depleted even than the reference and is therefore a bit denser. By contrast, the purely thermal models all have a higher and almost identical density in this depth range; the two high-density segments in models U-36/T and U-144/T downward from 100 km are due to eclogitic crustal material that is beginning to founder. The profiles for the 72 and 144 ppm water models look very similar and show the same features, except that they seem to reach a bit less deep;

the reason is probably that the generally lower viscosity in these models allows density anomalies to rise and spread out laterally more easily. The same pattern is observed in the models with earlier impact times.

As the thermoelastic model is based on an equation of state, it also provides the isothermal bulk modulus K_T directly, although it does not yet include the shear modulus and its derivatives. Nonetheless, as a first step toward application to seismic data, we calculate the bulk sound speed in the infinite-frequency approximation,

$$v_B = \sqrt{\frac{K_S}{\rho}} = \sqrt{v_P^2 - \frac{4}{3}v_S^2}; \tag{11}$$

the adiabatic bulk modulus K_S can be calculated directly from the available thermoelastic properties. This relation permits the direct comparison with data from a seismometer on Mars.

Figure 8 shows representative depth profiles of TC models from the 36 ppm water series. The profiles for models with impacts correspond to the impact site and show the signature of the remnants of the impact in the topmost mantle. The magnitude of the seismic anomaly can be assessed by comparison with the laterally averaged profile for model Ref-36, which is virtually identical with the laterally averaged profiles of the impact-affected models; the seismic v_B anomaly is on the order of a few tens of meters per second. The anomalies in the other model series are of a similar magnitude; as we did not consider possible effects of water due to limited data and the generally low water concentrations in these models, the water-related effects on seismic velocity are not included here, but would likely be negligible in our models. The seismic profile shows a slightly thickened crust at the impact site in models I-36 and U-36, but given the limitations on spatial resolution, the thickening should not be interpreted quantitatively.

4. Discussion

The most interesting dynamical feature of the models of this study are certain effects of the compositional contribution to the buoyancy of mantle material on the character of convection and the stability of the lithosphere, the asthenosphere, and local structures therein. *Plesa and Breuer* [2014] have studied the effect of different compositional density contrasts on convection in a more idealized Mars-like planet with imposed density contrasts and found that the depleted low-density layer is dynamically stable enough to suppress melting and crust formation to a significant extent and thus result in a thinner crust if the density difference between depleted material in the melting zone and fertile rock exceeds a certain value. Our models, in which the density contrast is not imposed but calculated from the compositional changes the mantle material undergoes upon melting, confirm the finding of those authors and suggest that in Mars density contrasts between fertile and depleted mantle rock may indeed reach a magnitude that throttles melt production. Moreover, local features with extreme density contrasts, exemplified here by anomalies created by basin-forming impacts, rise toward the base of the lithosphere, where they spread out under the influence of their own strong buoyancy. The long-lived compositional component of that buoyancy, which is not destroyed by diffusion, makes it possible for them to survive until they are integrated into the lithosphere, facilitating their preservation for the entire remaining history of the planet. *Rolf et al.* [2017] came to a similar conclusion in their models of the Moon.

As Mars has been hit by many impacts large enough to penetrate into the asthenosphere or even deeper, impacts should be expected to have produced substantial lateral chemical heterogeneity in the uppermost Martian mantle, because they would remelt material in the regular melting zone to different degrees according to their sizes and depths of penetration. The largest events would even affect mantle material that lies below the regular melting region and may therefore be more pristine. The resulting ancient melts from the impact would span a wide range of compositions. Moreover, their source regions in the mantle, which are depleted to different degrees, would themselves form a set of heterogeneous source regions for later volcanism if they become reactivated as melt sources, e.g., by plumes. All this heterogeneity may be reflected in the chemical variability observed in the different types of Martian meteorites. Although the impacts we have modeled postdate the supposed time around 4.5 Ga [e.g., *Borg et al.*, 1997, 2016] at which the major heterogeneity distinguishing the different classes of Martian meteorites was established by several hundred millions of years, the mechanism as such could have worked at those earlier times as well; the model pairs with impacts at earlier times indicate that it is viable even at the more vigorous convection when the lithosphere was thinner and the mantle even hotter, and the higher number of giant impacts would offer more opportunities

to form the corresponding strong anomalies. Such a scenario would come close to Option 3 of *Borg et al.* [2016, Figure 6], in which a major part of the mantle of the recently accreted and differentiated early Mars is molten during giant impacts and undergoes silicate differentiation, which produces separate shergottite and nakhlite source regions by ~4.5 Ga. Apart from these regional scenarios, we note that even regular melting could induce some degree of compositional layering with a density structure that counteracts rehomogenization, especially at higher initial temperatures than assumed here, as shown already before by *Plesa and Breuer* [2014]. That scenario resembles the one proposed by *Jones* [2003], who has suggested that the mantle sources of nakhlites and the more depleted shergottites lie at different depths and are largely isolated from each other. Finally, if a part of the impactor material merges with the mantle target, this effect may permit it to leave its signature in those preserved anomalies, although we did not include the potentially different composition of the impactor in the model.

Apart from the obvious crater at the surface, how can old impact sites be detected? The most conspicuous feature of an impact, the crater, is being obliterated with time and may all but disappear. Indeed, even for very large impacts, it is not quite clear how many have occurred in the ancient past of Mars: an analysis by *Frey* [2008] tallied 20 circular depressions with more than 1000 km diameter that are considered traces of giant impacts, whereas a more recent revision by *Frey and Mannoia* [2014] came up with 31 candidates. These analyses were based on topography, modeled crustal thicknesses, and surface geology, all of which depend on assumptions or may be affected by later influences such as rebound or the spreading and leveling of crustal thickness undulations. Under such circumstances, additional criteria provided by gravimetry or seismology could, in principle, be helpful.

Figure 7 shows some representative density profiles that quantify the density contrast that characterizes the self-stabilizing impact-created anomalies, which at that stage is entirely compositional. The present-day density deficit associated with very large impacts such as Isidis or even Utopia reaches its maximum of ~30 kg/m^3 at a depth of 120 or 220 km, respectively, and may be overlain by anomalous structures such as a thickened crust or a thin slice of less depleted mantle. Neglecting curvature, we make a rough estimate of the expected gravity anomaly by approximating the deficit mass of the mantle anomaly by a flat, thick cylinder of radius R_a, height h_a, and homogeneous density contrast $\Delta\varrho$ extending downward from a depth z_a. The vertical component of the gravity anomaly on its axis relative to the reference model mantle is given by

$$\Delta g_z = 2\pi G_0 \Delta\varrho \left(h_a + \sqrt{z_a^2 + R_a^2} - \sqrt{(z_a + h_a)^2 + R_a^2} \right) \tag{12}$$

and can reach values of −129 and −194 mgal for I-36/TC (h_a = 135 km, $R_a \approx \pi R_P/6$) and U-36/TC (h_a = 195 km, $R_a \approx \pi R_P/3$), respectively (Figure 9), assuming $\Delta\varrho = -25$ kg/m^3 and $z_a = 85$ km in both cases. We find a crust thickened by ~20 km in both impact models, but notice that the vertical resolution of our models does not permit a much better determination of the crustal thickness than the grid point spacing (~13 km). To estimate the crustal contribution, we construct a three-cylinder model consisting of a deep cylinder ($\Delta\varrho = -12$ or -20 kg/m^3 for Isidis and Utopia) representing the excess crust and two stacked cylinders ($\Delta\varrho$ = 10 or 250 kg/m^3) each spanning half of the depth range of normal crust and representing the denser, pore-free crust in the final crater; the radius of the crustal anomaly is taken to be that of the final crater. The resulting positive anomalies will result in fairly similar total gravity signals from these two impacts, and they would at any rate be visible from the ground as well as from an orbit at the elevation of the Mars Reconnaissance Orbiter (MRO) (~400 km) (Figure 9). However, due to the nonuniqueness of potential fields, such signatures cannot be taken as proof of the presence of an impact-related mantle anomaly. To illustrate this point, one can try to mimic the impact-generated mantle anomalies by crust thickened by a certain amount over an area of the dimensions of our assumed mantle anomaly but overlying an undisturbed mantle. As the gray curves labeled cqI-36 and cqU-36 in Figure 9 show, thickening by 15 or 22 km of a crust with $\Delta\varrho = -210$ kg/m^3 would almost perfectly match the I-36/TC and U-36/TC mantle anomalies, respectively. An important implication of this trade-off is that neglecting negative densities anomalies in the mantle such as those caused by ancient basin-forming impacts may result in an overestimate of the crustal thickness. However, we emphasize that this calculation for a thickened postimpact crust is only an example based on the larger impacts in this study; depending on the parameters of the impact, the postimpact crust could also be thinner. Net crustal thinning is often invoked in the interpretation of gravity signatures of impact basins. Therefore, our approach to extract almost all of the melt generated directly by the impact and assume that it contributes to the formation of the postimpact crust only puts an upper bound on the crustal thickness

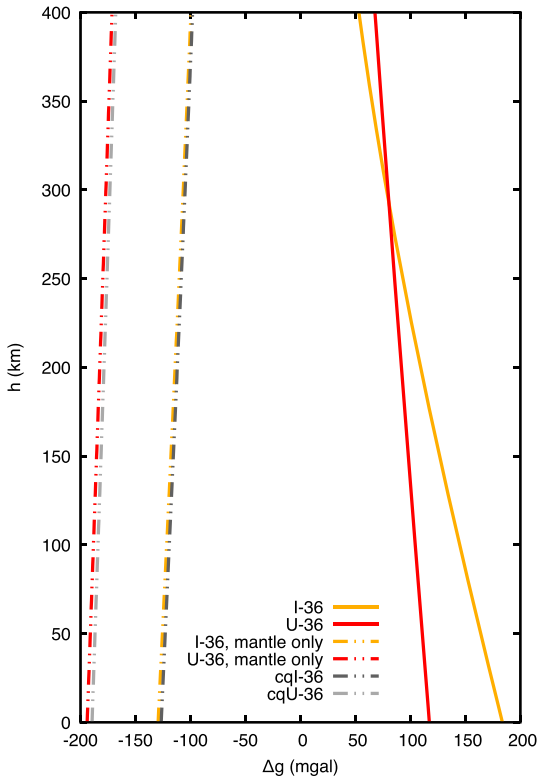

Figure 9. Estimated on-axis gravity anomaly at the TC models for I-36 and U-36 as a function of height above the Martian surface according to equation (12). Also shown are the signals of positive crustal thickness anomalies above normal mantle (cqI-36 and cqU-36) that would be almost identical to the impact-generated mantle anomalies in I-36 and U-36, respectively, as discussed in the text.

but may be an overestimate. The complex processes occurring during the rebound and collapse of the transient crater, the crystallization of a postimpact magma pond, and the different modes of melt migration under these conditions cannot be modeled within the framework of our global mantle convection models. Dedicated investigations of the impact process itself will be needed to provide a parameterization that allows to determine the fraction of impact-generated melt that actually forms new postimpact crust in a modeling setup like ours. At any rate, present models of the global crustal thickness variation on Mars [e.g., *Zuber et al.*, 2000; *Wieczorek and Zuber*, 2004] are based on the assumption of a constant mantle density beneath the crust and may therefore produce inaccurate thickness estimates.

A seismic survey targeted at a potential impact site will certainly map the crust–mantle boundary and thus resolve deviations in crustal thickness, but the detection of the bulk velocity anomaly in the mantle, which is not expected to exceed 50 m/s (cf. Figure 8), would require a very good coverage of the shallow mantle with seismic rays and a reliable reference model; whether actual *P* or *S* wave anomalies are more readily seen is yet to be investigated. Although such observations are in principle possible, the observational framework is not expected to come into existence in the next few decades.

The global surface heat flow curves are very similar for all models over almost the entire evolution of the planet, as we stuck to one radionuclide composition; this is in agreement with the findings by *Plesa et al.* [2015], who arrive at similar values for their models with the *Wänke and Dreibus* [1994] concentrations. The heat flow experiment HP^3 on the InSight mission, which is set to arrive at Mars in 2018, will hopefully answer the question whether the radionuclide composition by *Wänke and Dreibus* [1994] is correct, but it will not be able to discern between other characteristics of interior models such as viscosity or water content due to the insensitivity of q_s. Estimates of the elastic thickness of the lithosphere and the mean lithospheric heat flow, which are already available, are burdened with more assumptions but provide more means to distinguish between different scenarios, especially with regard to the water content and its effect on convective vigor. We did not consider local heat flow variations in more detail, because they are poorly resolved and depend on a variety of assumptions. For instance, local variations arise in our models as a consequence of crustal temperature modifications after impacts, whereas in the lunar models by *Rolf et al.* [2017], they are caused by variations in the thickness of ejecta layers with a low thermal conductivity. We agree with those authors in the sense that both of us assigned an insulating effect to ejecta or regolith in general, but contrary to *Rolf et al.* [2017], we assume that the permanent meteorite flux had produced an insulating global regolith layer from the beginning, which is implemented as a pressure-dependent layer of reduced thermal conductivity and density. Similar to them, we reset the porosity of the surface layer to zero within the final crater by invoking magmatic processes that fill the pore space; this results in positive mass anomalies in the crust within the crater. As it is impossible to quantify plausibly the ratio of intrusive to extrusive magmatism in the aftermath of the impact or the detailed temperature distribution of the ejecta and the newly formed crust in the framework

of these global models, we set the temperature of the crater infilling to the surface value as the simplest solution but caution that this results in an underestimate of the postimpact crustal temperature; the crater surface heat flows in Figure 6 should therefore be regarded as lower bounds. At any rate, local variations of conductivity at the surface are not expected to have any substantial effect on the dynamics and processes in the deeper interior, especially in the direct aftermath of the impact, and on the resulting density anomalies.

5. Conclusions

The compositional contribution to buoyancy in convection models with melting can produce a stable, depleted layer beneath the lithosphere that acts to reduce melt production and may help to establish separate chemical reservoirs. The same factor appears to be crucial for anchoring highly depleted compositional anomalies, which may for instance be produced by large impacts, beneath the lithosphere and stabilize them for time spans of hundreds of millions of years, allowing them to be permanently included into the growing lithosphere. Such stable anomalies may appear as different reservoirs in the geochemical record.

In spite of this mechanism of preservation, anomalies such as those created by giant impacts are heavily modified by mantle convection, and their geophysical signature is expected to degrade with time. As the chemical anomaly entails a density anomaly, it may be possible to detect it in gravity data; by contrast, the prospects for detecting it with seismic means seem rather poor, and the heat flux anomaly directly caused by the impact is nil. Thermal signals from single impacts up to the size considered here do not have a long-lasting, discernible effect on the global heat flow; whether that is different for the cumulative effects of several basin-forming impacts will depend on their magnitudes and timing and will be investigated in a future study.

Appendix A: Martian Mantle Solidus

We have revised the mantle solidus derived in *Ruedas et al.* [2013b], which was based on data by *Bertka and Holloway* [1994] and *Schmerr et al.* [2001] from experiments on a K-free Martian model peridotite similar to the compositional model from *Wänke and Dreibus* [1994]; we decided not to use the results from *Borg and Draper* [2003] and *Agee and Draper* [2004] although it would be desirable to have more data at higher p, because these authors used a material with somewhat different iron and alkali contents. More recently, *Matsukage et al.* [2013] and *Collinet et al.* [2015] performed new melting experiments on Martian mantle analogue materials after *Wänke and Dreibus* [1994], the former also on a K-free composition. As *Collinet et al.* [2015] pointed out, the lack of K in the other studies would lead to an increase of the solidus by ∼30 K; this estimate is consistent with the effect of K on the solidus observed in the K-doped peridotite from *Wang and Takahashi* [2000], if the difference in K content is accounted for by a linear dependence. Therefore, we reduced the temperature values measured at upper mantle pressures from the other studies by 30 K. As *Collinet et al.* [2015] did not provide subsolidus data, we extrapolated the melting degree–temperature relations from their experiments linearly at each pressure and weighted the resulting solidus estimate doubly. In view of the high-p values from *Schmerr et al.* [2001], it seems that the solidus determined by *Collinet et al.* [2015] themselves is unsuited for extrapolation beyond ∼3.5 GPa, and so we decided to fit a selection of all available data for pressures up to the appearance of pv + fp anew, which gave

$$T_s = \begin{cases} 0.118912p^3 - 6.37695p^2 + 130.33p + 1340.38 & \text{for } p < 23\ \text{GPa} \\ 62.5p + 975 & \text{otherwise,} \end{cases} \tag{A1}$$

for p in gigapascal and T_s in kelvin. The linear fit to the highest p points from *Schmerr et al.* [2001] for the pv + fp stability field was only slightly shifted to avoid a kink at the transition but was otherwise left unchanged from our previous work, because the depressing effect of K on the solidus was observed to disappear at lower mantle conditions [*Wang and Takahashi*, 2000]; in our work, we rarely approach the solidus at that depth anyway, and pv + fp does not appear at all in the models of this study.

Apart from the data for the solidus itself, the work of *Matsukage et al.* [2013] and *Collinet et al.* [2015] was also used to readjust estimates for the temperatures at which certain mineral phases are exhausted during melting, especially for the garnet stability field.

Kiefer et al. [2015] discussed the effect of Na, K, and Ca on the Martian solidus and proposed shifting the original terrestrial peridotite solidus by *Hirschmann* [2000] down by 35 K in order to account for that effect.

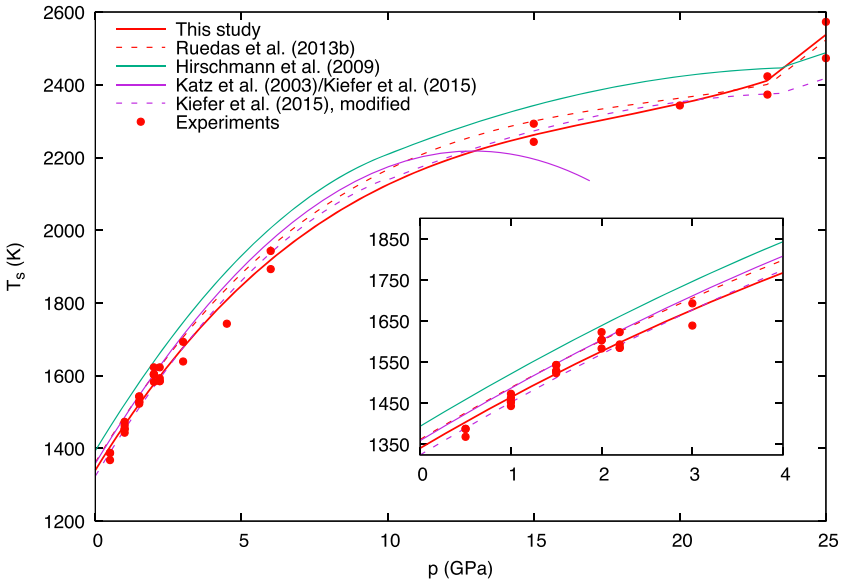

Figure A1. Different peridotite dry solidus functions. The experimental data are those used for fitting in this study, i.e., the data from *Bertka and Holloway* [1994], *Schmerr et al.* [2001], *Matsukage et al.* [2013] (all reduced by 30 K), and *Collinet et al.* [2015].

However, *Katz et al.* [2003, section 4.1] had already pointed out that the original *Hirschmann* [2000] solidus, which was based on intermediately fertile terrestrial compositions, seems to overestimate the solidus temperature as a consequence of the poor coverage of low-degree melting by experimental data and had suggested lowering it by 35 K, which they found to give a better fit to the experimental data; in other words, their improved fit for terrestrial peridotite is practically identical to the function *Kiefer et al.* [2015] suggest for Martian peridotite. Following the argument of *Kiefer et al.* [2015] concerning the effect of Na, K, and Ca, which is still valid, then implies that it is the function from *Katz et al.* [2003] that should be reduced by a further 35 K in order to produce a Martian solidus.

Figure A1 shows the functions proposed here and demonstrates that a further reduction of the *Kiefer et al.* [2015] solidus would result in a function that agrees very well with ours especially in the most critical pressure range up to 3 GPa. We have plotted the solidus from *Hirschmann et al.* [2009] instead of the one from *Hirschmann* [2000], because the former can be used at pressures above 10 GPa while being identical to the latter below that pressure. The solidus modified from *Kiefer et al.* [2015] applies the additional shift and uses the *Hirschmann et al.* [2009] solidus (shifted down by 70 K) at $p > 10$ GPa to make it applicable to higher pressures.

All of these solidi have used experimental data on nominally anhydrous materials. However, as recently pointed out by *Sarafian et al.* [2017], even nominally anhydrous samples that have been dried in order to remove water may still contain traces of it at the level of a few dozen or hundreds of parts per million. Those authors assert, on the basis of experiments of their own that apply a novel technique for monitoring water content, that previous studies systematically underestimated solidus temperatures because of such trace water. The considerations above concerning the shifts of the solidus due to compositional variations remain correct even if their conclusions are confirmed, but the true anhydrous solidus would then have to be determined by an additional correction that would counteract the depression caused by alkalis and iron. Specifically, for a pressure of 1.5 GPa, at which they conducted their experiments, they inferred a water content of 140 ppm in the nominally anhydrous samples on which the fit of the *Hirschmann* [2000] solidus was based and deduced that an increase of the solidus temperature by ∼60 K is necessary to correct this error. This would imply that the solidus originally determined by *Hirschmann et al.* [2009] for terrestrial anhydrous peridotite would in fact have to be lowered by a mere 10 K to apply to Mars. However, we think that the data to devise a more generally applicable correction are not yet sufficient at this point, and so we stick to the conventional data sets.

Appendix B: Estimate of the Geometrical Error in 2-D Global Mean Calculations

We consider a single axisymmetric anomaly on the surface of a spherical planet. In two dimensions, such an anomaly would be represented by a cross section through the center of the sphere and the center of the anomaly, and the anomaly would appear as an arc of length θ, i.e., it occupies a fraction $f_2 = \theta/(2\pi)$ of the perimeter of the cross section. By contrast, in three dimensions the anomaly is a spherical cap that occupies a fraction

$$f_3 = \frac{1}{4\pi}\int_0^{2\pi}\int_0^{\frac{\theta}{2}} \sin\theta \mathrm{d}\theta \mathrm{d}\varphi = \frac{1}{2}\left(1-\cos\frac{\theta}{2}\right) \tag{B1}$$

of the total surface of the sphere. Hence, the amplitude marking the impact in the two-dimensional model should be multiplied by a factor

$$\frac{f_3}{f_2} = \frac{\pi}{\theta}\left(1-\cos\frac{\theta}{2}\right), \tag{B2}$$

with θ in radians; the discrepancy is worst for small anomalies. For the Huygens, Isidis, and Utopia events, we have angles θ of 1.26°, 3.64°, and 9.1°, respectively, and so the correction factors would be 0.0086, 0.025, and 0.062, respectively.

Notation

The subscript "imp" indicates a property of the impactor throughout the text.

a, b	scaling and shift parameters for p_s after *Ruedas* [2017]
B	dislocation creep prefactor
c_p	heat capacity
C_i	concentration of i
D_f	final crater diameter
D_{imp}	impactor diameter
D_{tr}	transient crater diameter
$D_{s2c} \approx 5.6$ km	simple/complex transition crater diameter (Mars)
f	melting degree/depletion
$G_0 = 6.67408 \times 10^{-11}\ \mathrm{m^3/(kg\,s^2)}$	Newton's constant of gravitation
$g = 3.72\ \mathrm{m/s^2}$	surface gravity acceleration (Mars)
Δg_z	vertical component of gravity anomaly
K_S	adiabatic bulk modulus
n	decay exponent for p_s after *Ruedas* [2017]
p_{IM}	shock pressure from impedance-match solution
p_l	lithostatic pressure
p_s	peak shock pressure
Q	activation enthalpy
q_s	surface heat flow
$R_{\mathrm{gas}} = 8.3144598\ \mathrm{J/(mol\,K)}$	universal gas constant
$R_P = 3389.5$ km	planetary radius (Mars)
r_{infl}	radius of isobaric core defined by inflection point of p_s
r_{PVM}	radius of isobaric core after *Pierazzo et al.* [1997]
Ra_0, Ra_{eff}	initial, effective Rayleigh number
S_h	Hugoniot slope
T	temperature
$T_{\mathrm{pot}} = 1700$ K	initial potential temperature
T_s	solidus temperature
u_{IM}	particle velocity from impedance-match solution
v_B	speed of sound
$v_{\mathrm{imp}} = 9.6$ km/s, $v_{z,\mathrm{imp}} = 6.8$ km/s	impact velocity and its vertical component (Mars)
v_P, v_S	P, S wave velocity
z_{el}	elastic thickness of the lithosphere

z_{ic}	depth to center of isobaric core
$\dot{\epsilon} = 10^{-17}$ s^{-1}	strain rate
η_{mean}	volumetric mean of viscosity, nondimensionalized
φ	porosity
$\varphi_r = 0.007$	threshold porosity for melt extraction
γ	Grüneisen parameter
ν	exponent of creep law
ϱ	density
$\sigma_y = 15$ MPa	yield stress

Acknowledgments
Anne Hofmeister and Zhicheng Jing kindly gave additional explanations of various aspects of their respective work. We thank Martin Knapmeyer for helpful remarks on some seismological aspects and Sabrina Schwinger for helping to clarify a question concerning the water content of the crust. The comments by Gregor Golabek and an anonymous referee are gratefully acknowledged. T.R. was supported by grant Ru 1839/1-1 from the Deutsche Forschungsgemeinschaft (DFG), with additional initial funding from the Helmholtz Alliance project "Planetary evolution and life." D.B. was supported by the DFG (SFB-TRR 170). This is TRR 170 publication no. 28. The numerical calculations were carried out on the computational resource ForHLR II at the Steinbuch Centre for Computing, Karlsruhe Institute of Technology, funded by the Ministry of Science, Research and the Arts Baden-Württemberg and DFG. Some earlier code development first applied in this study benefitted from support by the NASA Planetary Geology and Geophysics Program through grant NNX11AC62G and the use of computing resources provided by the NASA High-End Computing (HEC) Program through the NASA Center for Climate Simulation (NCCS) at Goddard Space Flight Center, award SMD-11-2549. T.R. is grateful to Sean Solomon for having made this support from NASA possible. The data used in this investigation are presented in this paper and the supporting information; data sets used in plots and figures can be obtained from Figshare at https://doi.org/10.6084/m9.figshare.c.3777686.

References

Abramov, O., S. M. Wong, and D. A. Kring (2012), Differential melt scaling for oblique impacts on terrestrial planets, *Icarus*, *218*(2), 906–916, doi:10.1016/j.icarus.2011.12.022.

Abramowitz, M., and I. A. Stegun (Eds.) (1964), *Handbook of Mathematical Functions*, U.S. National Bureau of Standards, Dover Publ., New York.

Agee, C. B., and D. S. Draper (2004), Experimental constraints on the origin of Martian meteorites and the composition of the Martian mantle, *Earth Planet. Sci. Lett.*, *224*(3–4), 415–429.

Ashcroft, N. W., and N. D. Mermin (1976), *Solid State Physics*, Saunders College Publ., Fort Worth, Tex.

Aubaud, C., E. H. Hauri, and M. M. Hirschmann (2004), Hydrogen partition coefficients between nominally anhydrous minerals and basaltic melts, *Geophys. Res. Lett.*, *31*, L20611, doi:10.1029/2004GL021341.

Balog, P. S., R. A. Secco, and D. C. Rubie (2001), Density measurements of liquids at high pressure: Modifications to the sink/float method by using composite spheres, and application to Fe-10 wt%S, *High Press. Res.*, *21*(5), 237–261, doi:10.1080/08957950108201026.

Balog, P. S., R. A. Secco, D. C. Rubie, and D. J. Frost (2003), Equation of state of liquid Fe-10 wt % S: Implications for the metallic cores of planetary bodies, *J. Geophys. Res.*, *108*(B2), 2124, doi:10.1029/2001JB001646.

Barnett, D. N., and F. Nimmo (2002), Strength of faults on Mars from MOLA topography, *Icarus*, *157*(1), 34–42, doi:10.1006/icar.2002.6817.

Belleguic, V., P. Lognonné, and M. Wieczorek (2005), Constraints on the Martian lithosphere from gravity and topography data, *J. Geophys. Res.*, *110*, E11005, doi:10.1029/2005JE002437.

Berryman, J. G. (1995), Mixture theories for rock properties, in *Rock Physics & Phase Relations—A Handbook of Physical Constants, AGU Reference Shelf*, vol. 3, edited by T. J. Ahrens, pp. 205–228, AGU, Washington, D. C.

Bertka, C. M., and Y. Fei (1998), Density profile of an SNC model Martian interior and the moment-of-inertia factor of Mars, *Earth Planet. Sci. Lett.*, *157*(1–2), 79–88, doi:10.1016/S0012-821X(98)00030-2.

Bertka, C. M., and J. R. Holloway (1994), Anhydrous partial melting of an iron-rich mantle I: Subsolidus phase assemblages and partial melting phase relations at 10 to 30 kbar, *Contrib. Mineral. Petrol.*, *115*(3), 313–322.

Bjorkman, M. D., and K. A. Holsapple (1987), Velocity scaling impact melt volume, *Int. J. Impact Eng.*, *5*(1–4), 155–163, doi:10.1016/0734-743X(87)90035-2.

Blundy, J., and B. Wood (2003), Mineral–melt partitioning of uranium, thorium and their daughters, in *Uranium-Series Geochemistry, no. 52 in Rev. Mineral. Geochem.*, edited by B. Bourdon et al., pp. 59–123, Mineral. Soc. of Am., Washington, D. C.

Blundy, J. D., T. J. Falloon, B. J. Wood, and J. A. Dalton (1995), Sodium partitioning between clinopyroxene and silicate melts, *J. Geophys. Res.*, *100*(B8), 15,501–15,515.

Bolfan-Casanova, N., H. Keppler, and D. C. Rubie (2000), Water partitioning between nominally anhydrous minerals in the MgO-SiO_2–H_2O system up to 24 GPa: Implications for the distribution of water in the Earth's mantle, *Earth Planet. Sci. Lett.*, *182*, 209–221.

Borg, L., L. E. Nyquist, L. A. Taylor, H. Weismann, and C.-Y. Shih (1997), Constraints on Martian differentiation processes from Rb-Sr and Sm-Nd isotopic analyses of the basaltic shergottite QUE 94201, *Geochim. Cosmochim. Acta*, *61*(22), 4915–4931.

Borg, L. E., and D. S. Draper (2003), A petrogenetic model for the origin and compositional variation of the Martian basaltic meteorites, *Meteorit. Planet. Sci.*, *38*(12), 1713–1731.

Borg, L. E., G. A. Brennecka, and S. J. K. Symes (2016), Accretion timescale and impact history of Mars deduced from the isotopic systematics of Martian meteorites, *Geochim. Cosmochim. Acta*, *175*, 150–167, doi:10.1016/j.gca.2015.12.002.

Breuer, D., A.-C. Plesa, N. Tosi, and M. Grott (2016), Water in the Martian interior—The geodynamical perspective, *Meteorit. Planet. Sci.*, *51*(11), 1959–1992, doi:10.1111/maps.12727.

Brey, G. P., and T. Köhler (1990), Geothermobarometry in four-phase lherzolites II. New thermobarometers, and practical assessment of existing thermobarometers, *J. Petrol.*, *31*(6), 1353–1378, doi:10.1093/petrology/31.6.1353.

Brooker, R. A., Z. Du, J. D. Blundy, S. P. Kelley, N. L. Allan, B. J. Wood, E. M. Chamorro, J.-A. Wartho, and J. A. Purton (2003), The 'zero charge' partitioning behaviour of noble gases during mantle melting, *Nature*, *423*, 738–741, doi:10.1038/nature01708.

Chamorro, E. M., R. A. Brooker, J.-A. Wartho, B. J. Wood, S. P. Kelley, and J. D. Blundy (2002), Ar and K partitioning between clinopyroxene and silicate melt to 8 GPa, *Geochim. Cosmochim. Acta*, *66*(3), 507–519.

Chen, J., T. Inoue, H. Yurimoto, and D. Weidner (2002), Effect of water on olivine-wadsleyite phase boundary in the $(Mg, Fe)_2SiO_4$ system, *Geophys. Res. Lett.*, *29*(18), 1875, doi:10.1029/2001GL014429.

Collinet, M., E. Médard, B. Charlier, J. Vander Auwera, and T. L. Grove (2015), Melting of the primitive Martian mantle at 0.5–2.2 GPa and the origin of basalts and alkaline rocks on Mars, *Earth Planet. Sci. Lett.*, *427*, 83–94, doi:10.1016/j.epsl.2015.06.056.

Corgne, A., and B. J. Wood (2004), Trace element partitioning between majoritic garnet and silicate melt at 25 GPa, *Phys. Earth Planet. Inter.*, *143-144*, 407–419, doi:10.1016/j.pepi.2003.08.012.

Croft, S. K. (1980), Cratering flow fields: Implications for the excavation and transient expansion stages of crater formation, in *11th Lunar and Planetary Science Conference*, pp. 2347–2378, Pergamon Press, New York.

Debye, P. (1912), Zur Theorie der spezifischen Wärme, *Ann. Phys.*, *IV/39*, 789–839.

Duffy, T. S., and D. L. Anderson (1989), Seismic velocities in mantle minerals and the mineralogy of the upper mantle, *J. Geophys. Res.*, *94*(B2), 1895–1912.

Dygert, N., Y. Liang, C. Sun, and P. Hess (2014), An experimental study of trace element partitioning between augite and Fe-rich basalts, *Geochim. Cosmochim. Acta*, *132*, 170–186, doi:10.1016/j.gca.2014.01.042, 10.1016/j.gca.2014.09.013.

Fernández, Y. R., J.-Y. Li, E. S. Howell, and L. M. Woodney (2015), Asteroids and comets, in *Physics of Terrestrial Planets and Moons, Treatise on Geophysics*, vol. 10, 2nd ed., edited by T. Spohn, chap. 10.15, pp. 487–528, Elsevier, Amsterdam.

Fornberg, B. (1998), Calculation of weights in finite difference formulas, *SIAM Rev.*, *40*(3), 685–691.

Frey, H. (2008), Ages of very large impact basins on Mars: Implications for the late heavy bombardment in the inner solar system, *Geophys. Res. Lett.*, *35*, L13203, doi:10.1029/2008GL033515.

Frey, H. V., and L. M. Mannoia (2014), A revised, rated and dated inventory of very large candidate impact basins on Mars, *Lunar Planet. Sci.*, *45*, 1892.

Gault, D. E., and E. D. Heitowit (1963), The partition of energy for hypervelocity impact craters formed in rock, in *Proceedings of the 6th Hypervelocity Impact Symposium*, vol. 2, pp. 419–456, U.S. Army, U.S. Air Force, U.S. Navy, Cleveland, Ohio.

Gault, D. E., and J. A. Wedekind (1978), Experimental studies of oblique impact, *Proc. Lunar Planet. Sci. Conf.*, *9*, 3843–3875.

Golabek, G. J., T. Keller, T. V. Gerya, G. Zhu, P. J. Tackley, and J. A. D. Connolly (2011), Origin of the Martian dichotomy and Tharsis from a giant impact causing massive magmatism, *Icarus*, *215*(1), 346–357, doi:10.1016/j.icarus.2011.06.012.

Grott, M., and D. Breuer (2008), The evolution of the Martian elastic lithosphere and implications for crustal and mantle rheology, *Icarus*, *193*(2), 503–515.

Grüneisen, E. (1912), Theorie des festen Zustandes einatomiger Elemente, *Ann. Phys.*, *39*, 257–306.

Grüneisen, E. (1926), Zustand des festen Körpers, in *Thermische Eigenschaften der Stoffe, Handbuch der Physik*, vol.10, edited by C. Drucker et al., pp. 1–59, Springer, Heidelberg.

Harlow, G. E. (1997), K in clinopyroxene at high pressure and temperature: An experimental study, *Am. Mineral.*, *82*(3–4), 259–269.

Hauck, S. A., and R. J. Phillips (2002), Thermal and crustal evolution of Mars, *J. Geophys. Res.*, *107*(E7), 5052, doi:10.1029/2001JE001801.

Hauri, E. H., T. P. Wagner, and T. L. Grove (1994), Experimental and natural partitioning of Th, U, Pb and other trace elements between garnet, clinopyroxene and basaltic melts, *Chem. Geol.*, *117*, 149–166.

Hauri, E. H., G. A. Gaetani, and T. H. Green (2006), Partitioning of water during melting of the Earth's upper mantle at H_2O-undersaturated conditions, *Earth Planet. Sci. Lett.*, *248*(3–4), 715–734.

Head, J. W., and L. Wilson (1992), Magma reservoirs and neutral buoyancy zones on Venus: Implications for the formation and evolution of volcanic landforms, *J. Geophys. Res.*, *97*(E3), 3877–3903, doi:10.1029/92JE00053.

Hernlund, J. W., and P. J. Tackley (2008), Modeling mantle convection in the spherical annulus, *Phys. Earth Planet. Inter.*, *171*(1–4), 48–54, doi:10.1016/j.pepi.2008.07.037.

Hirschmann, M. M. (2000), Mantle solidus: Experimental constraints and the effects of peridotite composition, *Geochem. Geophys. Geosyst.*, *1*, 1042, doi:10.1029/2000GC000070.

Hirschmann, M. M., T. Tenner, C. Aubaud, and A. C. Withers (2009), Dehydration melting of nominally anhydrous mantle: The primacy of partitioning, *Phys. Earth Planet. Inter.*, *176*(1–2), 54–68.

Hirth, G., and D. L. Kohlstedt (2003), Rheology of the upper mantle and the mantle wedge: A view from the experimentalists, in *Inside the Subduction Factory, Geophys. Monogr.*, vol. 138, edited by J. Eiler, pp. 83–105, AGU, Washington, D. C.

Hofmeister, A. M. (1999), Mantle values of thermal conductivity and the geotherm from phonon lifetimes, *Science*, *283*, 1699–1706.

Hofmeister, A. M., and J. M. Branlund (2015), Thermal conductivity of the Earth, in *Mineral Physics, Treatise on Geophysics*, vol. 2, 2nd ed., edited by G. D. Price and L. Stixrude, chap. 2.23, pp. 583–608, Elsevier, Amsterdam, doi:10.1016/B978-0-444-53802-4.00047-6.

Ita, J., and L. Stixrude (1992), Petrology, elasticity, and composition of the mantle transition zone, *J. Geophys. Res.*, *97*(B5), 6849–6866.

Ivanov, B. A. (2001), Mars/Moon cratering rate ratio estimates, *Space Sci. Rev.*, *96*(1–4), 87–104, doi:10.1023/A:1011941121102.

Jin, Z.-M., J. Zhang, H. W. Green II, and S. Jin (2001), Eclogite rheology: Implications for subducted lithosphere, *Geology*, *29*(8), 667–670.

Jing, Z., and S.-i. Karato (2009), The density of volatile bearing melts in the Earth's deep mantle: The role of chemical composition, *Chem. Geol.*, *262*(1–2), 100–107.

Jing, Z., and S.-i. Karato (2011), A new approach to the equation of state of silicate melts: An application of the theory of hard sphere mixtures, *Geochim. Cosmochim. Acta*, *75*(22), 6780–6802, doi:10.1016/j.gca.2011.09.004.

Jing, Z., and S.-i. Karato (2012), Effect of H_2O on the density of silicate melts at high pressures: Static experiments and the application of a modified hard-sphere model of equation of state, *Geochim. Cosmochim. Acta*, *85*, 357–372, doi:10.1016/j.gca.2012.03.001.

Johnson, B. C., T. J. Bowling, and H. J. Melosh (2014), Jetting during vertical impacts of spherical projectiles, *Icarus*, *238*, 13–22, doi:10.1016/j.icarus.2014.05.003.

Jones, J. H. (1995), Experimental trace element partitioning, in *Rock Physics and Phase Relations — A Handbook of Physical Constants, AGU Reference Shelf*, vol. 3, edited by T. J. Ahrens, pp. 73–104, AGU, Washington, D. C.

Jones, J. H. (2003), Constraints on the structure of the Martian interior determined from the chemical and isotopic systematics of SNC meteorites, *Meteorit. Planet. Sci.*, *38*(12), 1807–1814.

Kaiura, G. H., and J. M. Toguri (1979), Densities of the molten FeS, FeS-Cu_2S and Fe–S–O systems—Utilizing a bottom-balance Archimedean technique, *Can. Metal. Q.*, *18*(2), 155–164, doi:10.1179/cmq.1979.18.2.155.

Katz, R. F., M. Spiegelman, and C. Langmuir (2003), A new parameterization of hydrous mantle melting, *Geochem. Geophys. Geosyst.*, *4*(9), 1073, doi:10.1029/2002GC000433.

Keller, T., and P. J. Tackley (2009), Towards self-consistent modeling of the Martian dichotomy: The influence of one-ridge convection on crustal thickness distribution, *Icarus*, *202*(2), 429–443, doi:10.1016/j.icarus.2009.03.029.

Khan, A., and J. A. D. Connolly (2008), Constraining the composition and thermal state of Mars from inversion of geophysical data, *J. Geophys. Res.*, *113*, E07003, doi:10.1029/2007JE002996.

Kiefer, W. S. (2003), Melting in the Martian mantle: Shergottite formation and implications for present-day mantle convection on Mars, *Meteorit. Planet. Sci.*, *38*(12), 1815–1832.

Kiefer, W. S., J. Filiberto, C. Sandu, and Q. Li (2015), The effects of mantle composition on the peridotite solidus: Implications for the magmatic history of Mars, *Geochim. Cosmochim. Acta*, *162*, 247–258, doi:10.1016/j.gca.2015.02.010.

Koga, K., E. Hauri, M. M. Hirschmann, and D. Bell (2003), Hydrogen concentration analyses using SIMS and FTIR: Comparison and calibration for nominally anhydrous minerals, *Geochem. Geophys. Geosyst.*, *4*(2), doi:10.1029/2002GC000378.

Konopliv, A. S., S. W. Asmar, W. M. Folkner, Ö. Karatekin, D. C. Nunes, S. E. Smrekar, C. F. Yoder, and M. T. Zuber (2011), Mars high resolution gravity fields from MRO, Mars seasonal gravity, and other dynamical parameters, *Icarus*, *211*(1), 401–428, doi:10.1016/j.icarus.2010.10.004.

Landwehr, D., J. Blundy, E. M. Chamorro-Perez, E. Hill, and B. Wood (2001), U-series disequilibria generated by partial melting of spinel lherzolite, *Earth Planet. Sci. Lett.*, *188*(3–4), 329–348, doi:10.1016/S0012-821X(01)00328-4.

Langmuir, C. H., E. M. Klein, and T. Plank (1992), Petrological systematics of mid-ocean ridge basalts: Constraints on melt generation beneath ocean ridges, in *Mantle Flow and Melt Generation at Mid-ocean Ridges*, vol. 71, edited by J. P. Morgan, D. K. Blackman, and J. Sinton, pp. 183–280, AGU, Washington, D. C.

Leone, G., L. Wilson, and A. G. Davies (2011), The geothermal gradient of Io: Consequences for lithosphere structure and volcanic eruptive activity, *Icarus*, *211*(1), 623–635, doi:10.1016/j.icarus.2010.10.016.

Li, Q., and W. S. Kiefer (2007), Mantle convection and magma production on present-day Mars: Effects of temperature-dependent rheology, *Geophys. Res. Lett.*, *34*, L16203, doi:10.1029/2007GL030544.

Mackwell, S. J., M. E. Zimmerman, and D. L. Kohlstedt (1998), High-temperature deformation of dry diabase with application to tectonics on Venus, *J. Geophys. Res.*, *103*(B1), 975–984.

Mamedov, B. A., E. Eser, H. Koç, and I. M. Askerov (2009), Accurate evaluation of the specific heat capacity of solids and its application to MgO and ZnO crystals, *Int. J. Thermophys.*, *30*(3), 1048–1054.

Matsukage, K. N., Y. Nagayo, M. L. Whitaker, E. Takahashi, and T. Kawasaki (2013), Melting of the Martian mantle from 1.0 to 4.5 GPa, *J. Miner. Petr. Sci.*, *108*(4), 201–214, doi:10.2465/jmps.120820.

Maxwell, D. E. (1977), Simple Z model of cratering, ejection, and the overturned flap, in *Impact and Explosion Cratering*, edited by D. J. Roddy, R. O. Pepin, and R. B. Merrill, pp. 1003–1008, Pergamon Press, New York.

McCubbin, F. M., A. Smirnov, H. Nekvasil, J. Wang, E. Hauri, and D. H. Lindsley (2010), Hydrous magmatism on Mars: A source for water for the surface and subsurface during the Amazonian, *Earth Planet. Sci. Lett.*, *292*(1–2), 132–138.

McCubbin, F. M., E. H. Hauri, S. M. Elardo, K. E. Vander Kaaden, J. Wang, and C. K. Shearer Jr. (2012), Hydrous melting of the Martian mantle produced both depleted and enriched shergottites, *Geology*, *40*(8), 683–686, doi:10.1130/G33242.1.

McCubbin, F. M., J. W. Boyce, P. Srinivasan, A. R. Santos, S. M. Elardo, J. Filiberto, A. Steele, and C. K. Shearer (2016), Heterogeneous distribution of H_2O in the Martian interior: Implications for the abundance of H_2O in depleted and enriched mantle sources, *Meteorit. Planet. Sci.*, *51*(11), 2036–2060, doi:10.1111/maps.12639.

McGovern, P. J., S. C. Solomon, D. E. Smith, M. T. Zuber, M. Simons, M. A. Wieczorek, R. J. Phillips, G. A. Neumann, O. Aharonson, and J. W. Head (2004), Localized gravity/topography admittance and correlation spectra on Mars: Implications for regional and global evolution, *J. Geophys. Res.*, *107*, E07007, doi:10.1029/2004JE002286.

Melosh, H. J. (1989), Impact cratering: A geologic process, in *Oxford Monographs on Geology and Geophysics*, 245 pp., Oxford Univ. Press, New York.

Melosh, H. J. (2011), Planetary surface processes, in *Cambridge Planetary Science*, Cambridge Univ. Press, Cambridge, U. K.

Mibe, K., Y. Orihashi, S. Nakai, and T. Fujii (2006), Element partitioning between transition-zone minerals and ultramafic melt under hydrous conditions, *Geophys. Res. Lett.*, *33*, L16307, doi:10.1029/2006GL026999.

Monteux, J., and J. Arkani-Hamed (2016), Scaling laws of impact induced shock pressure and particle velocity in planetary mantle, *Icarus*, *264*, 246–256, doi:10.1016/j.icarus.2015.09.040.

Morschhauser, A., M. Grott, and D. Breuer (2011), Crustal recycling, mantle dehydration, and the thermal evolution of Mars, *Icarus*, *212*(2), 541–558, doi:10.1016/j.icarus.2010.12.028.

Nimmo, F., G. D. Price, J. Brodholt, and D. Gubbins (2004), The influence of potassium on core and geodynamo evolution, *Geophys. J. Int.*, *156*(2), 363–376.

Nishida, K., E. Ohtani, S. Urakawa, A. Suzuki, T. Sakamaki, H. Terasaki, and Y. Katayama (2011), Density measurement of liquid FeS at high pressures using synchrotron X-ray absorption, *Am. Mineral.*, *96*(5–6), 864–868.

Novella, D., D. J. Frost, E. H. Hauri, H. Bureau, C. Raepsaet, and M. Roberge (2014), The distribution of H_2O between silicate melt and nominally anhydrous peridotite and the onset of hydrous melting in the deep upper mantle, *Earth Planet. Sci. Lett.*, *400*, 1–13, doi:10.1016/j.epsl.2014.05.006.

Ogawa, M., and T. Yanagisawa (2011), Numerical models of Martian mantle evolution induced by magmatism and solid-state convection beneath stagnant lithosphere, *J. Geophys. Res.*, *116*, E08008, doi:10.1029/2010JE003777.

Ogawa, M., and T. Yanagisawa (2012), Two-dimensional numerical studies on the effects of water on Martian mantle evolution induced by magmatism and solid-state mantle convection, *J. Geophys. Res.*, *117*, E06004, doi:10.1029/2012JE004054.

Ohtani, E., H. Mizobata, and H. Yurimoto (2000), Stability of dense hydrous magnesium silicate phases in the systems $Mg2SiO_4$–H_2O and $MgSiO_3$–H_2O at pressures up to 27 GPa, *Phys. Chem. Min.*, *27*(8), 533–544, doi:10.1007/s002690000097.

O'Keefe, J. D., and T. J. Ahrens (1985), Impact and explosion crater ejecta, fragment size, and velocity, *Icarus*, *62*(2), 328–338, doi:10.1016/0019-1035(85)90128-9.

O'Keefe, J. D., and T. J. Ahrens (1987), The size distributions of fragments ejected at a given velocity from impact craters, *Int. J. Impact Engng.*, *5*(1–4), 493–499, doi:10.1016/0734-743X(87)90064-9.

O'Leary, J. A., G. A. Gaetani, and E. H. Hauri (2010), The effect of tetrahedral Al^{3+} on the partitioning of water between clinopyroxene and silicate melt, *Earth Planet. Sci. Lett.*, *297*(1–2), 111–120.

Phillips, R. J., et al. (2008), Mars north polar deposits: Stratigraphy, age, and geodynamical response, *Science*, *320*(5880), 1182–1185, doi:10.1126/science.1157546.

Pierazzo, E., A. M. Vickery, and H. J. Melosh (1997), A reevaluation of impact melt production, *Icarus*, *127*(2), 408–423, doi:10.1006/icar.1997.5713.

Plesa, A.-C., and D. Breuer (2014), Partial melting in one-plate planets: Implications for thermo-chemical and atmospheric evolution, *Planet. Space Sci.*, *98*, 50–65, doi:10.1016/j.pss.2013.10.007.

Plesa, A.-C., N. Tosi, M. Grott, and D. Breuer (2015), Thermal evolution and Urey ratio of Mars, *J. Geophys. Res. Planets*, *120*(5), 995–1010, doi:10.1002/2014JE004748.

Poirier, J.-P. (2000), *Introduction to the Physics of the Earth's Interior*, 2nd ed., Cambridge Univ. Press, Cambridge, U. K.

Potter, R. W. K., D. A. Kring, and G. S. Collins (2015), Scaling of basin-sized impacts and the influence of target temperature, in *Large Meteorite Impacts and Planetary Evolution V, Geol. Soc. Am. Spec. Pap., 518*, edited by G. R. Osinski and D. A. Kring, pp. 99–113, doi:10.1130/2015.2518(06).

Råheim, A., and D. H. Green (1974), Experimental determination of the temperature and pressure dependence of the Fe-Mg partition coefficient for coexisting garnet and clinopyroxene, *Contrib. Mineral. Petrol.*, *48*(3), 179–203.

Reese, C. C., and V. S. Solomatov (2006), Fluid dynamics of local Martian magma oceans, *Icarus*, *184*(1), 102–120.

Reese, C. C., V. S. Solomatov, and J. R. Baumgardner (2002), Survival of impact-induced thermal anomalies in the Martian mantle, *J. Geophys. Res.*, *107*(E10), 5082, doi:10.1029/2000JE001474.

Reese, C. C., V. S. Solomatov, J. R. Baumgardner, D. R. Stegman, and A. V. Vezolainen (2004), Magmatic evolution of impact-induced Martian mantle plumes and the origin of Tharsis, *J. Geophys. Res.*, *109*, E08009, doi:10.1029/2003JE002222.

Richardson, J. E., H. J. Melosh, C. M. Lisse, and B. Carcich (2007), A ballistics analysis of the Deep Impact ejecta plume: Determining Comet Tempel 1's gravity, mass, and density, *Icarus*, *190*(2), 357–390, doi:10.1016/j.icarus.2007.08.001.

Ritzer, A., and S. A. Hauck (2009), Lithospheric structure and tectonics at Isidis Planitia, Mars, *Icarus*, *201*(2), 528–539, doi:10.1016/j.icarus.2009.01.025.

Rivoldini, A., T. Van Hoolst, O. Verhoeven, A. Mocquet, and V. Dehant (2011), Geodesy constraints on the interior structure and composition of Mars, *Icarus*, *213*(2), 451–472, doi:10.1016/j.icarus.2011.03.024.

Robbins, S. J., and B. M. Hynek (2012), A new global database of Mars impact craters ≥1 km: 2. Global crater properties and regional variations of the simple-to-complex transition diameter, *J. Geophys. Res.*, *117*(E6), E06001, doi:10.1029/2011JE003967.

Roberts, J. H., and J. Arkani-Hamed (2012), Impact-induced mantle dynamics on Mars, *Icarus*, *218*(1), 278–289, doi:10.1016/j.icarus.2011.11.038.

Roberts, J. H., R. J. Lillis, and M. Manga (2009), Giant impacts on early Mars and the cessation of the Martian dynamo, *J. Geophys. Res.*, *114*, E04009, doi:10.1029/2008JE003287.

Rolf, T., M.-H. Zhu, K. Wünnemann, and S. C. Werner (2017), The role of impact bombardment history in lunar evolution, *Icarus*, *286*, 138–152, doi:10.1016/j.icarus.2016.10.007.

Ruedas, T. (2017), Globally smooth approximations for shock pressure decay in impacts, *Icarus*, *289*, 22–33, doi:10.1016/j.icarus.2017.02.008.

Ruedas, T., P. J. Tackley, and S. C. Solomon (2013a), Thermal and compositional evolution of the Martian mantle: Effect of water, *Phys. Earth Planet. Inter.*, *220*, 50–72, doi:10.1016/j.pepi.2013.04.006.

Ruedas, T., P. J. Tackley, and S. C. Solomon (2013b), Thermal and compositional evolution of the Martian mantle: Effects of phase transitions and melting, *Phys. Earth Planet. Inter.*, *216*, 32–58, doi:10.1016/j.pepi.2012.12.002.

Sanloup, C., F. Guyot, P. Gillet, G. Fiquet, M. Mezouar, and I. Martinez (2000), Density measurements of liquid Fe-S alloys at high-pressure, *Geophys. Res. Lett.*, *27*(6), 811–814, doi:10.1029/1999GL008431.

Sarafian, E., G. A. Gaetani, E. H. Hauri, and A. R. Sarafian (2017), Experimental constraints on the damp peridotite solidus and oceanic mantle potential temperature, *Science*, *355*(6328), 942–945, doi:10.1126/science.aaj2165.

Schmerr, N. C., Y. Fei, and C. Bertka (2001), Extending the solidus for a model iron-rich Martian mantle composition to 25 GPa, in *32nd Annual Lunar and Planetary Science Conference*, Abstract 1157, Lunar and Planetary Science, Houston, Tex.

Schott, B., A. P. van den Berg, and D. A. Yuen (2001), Focussed time-dependent Martian volcanism from chemical differentiation coupled with variable thermal conductivity, *Geophys. Res. Lett.*, *28*(22), 4271–4274.

Schultz, P. H., and H. Glicken (1979), Impact crater and basin control of igneous processes on Mars, *J. Geophys. Res.*, *84*(B14), 8033–8047, doi:10.1029/JB084iB14p08033.

Shannon, R. D. (1993), Dielectric polarizabilities of ions in oxides and fluorides, *J. Appl. Phys.*, *73*(1), 348–366, doi:10.1063/1.353856.

Shaw, D. M. (2000), Continuous (dynamic) melting theory revisited, *Can. Mineral.*, *38*(5), 1041–1063.

Spudis, P. D. (1993), *The Geology of Multi-ring Impact Basins*, Cambridge Univ. Press, Cambridge, U. K.

Stacey, F. D. (1998), Thermoelasticity of a mineral composite and a reconsideration of lower mantle properties, *Phys. Earth Planet. Inter.*, *106*, 219–236.

Stacey, F. D., and P. M. Davis (2004), High pressure equations of state with applications to the lower mantle and core, *Phys. Earth Planet. Inter.*, *142*(3–4), 137–184, doi:10.1016/j.pepi.2004.02.003.

Stixrude, L., and M. S. T. Bukowinski (1990), Fundamental thermodynamic relations and silicate melting with implications for the constitution of D'', *J. Geophys. Res.*, *95*(B12), 19,311–19,325.

Tackley, P. J. (1996), Effects of strongly variable viscosity on three-dimensional compressible convection in planetary mantles, *J. Geophys. Res.*, *101*(B2), 3311–3332.

Tackley, P. J. (2008), Modelling compressible mantle convection with large viscosity contrasts in a three-dimensional spherical shell using the yin-yang grid, *Phys. Earth Planet. Inter.*, *171*(1–4), 7–18.

Tauber, M. E., D. B. Kirk, and D. E. Gault (1978), An analytic study of impact ejecta trajectories in the atmospheres of Venus, Mars, and Earth, *Icarus*, *33*, 529–536, doi:10.1016/0019-1035(78)90188-4.

Taura, H., H. Yurimoto, K. Kurita, and S. Sueno (1998), Pressure dependence on partition coefficients for trace elements between olivine and the coexisting melts, *Phys. Chem. Min.*, *25*(7), 469–484, doi:10.1007/s002690050138.

Taylor, S. R., and S. M. McLennan (2009), *Planetary Crusts*, 400 pp., Cambridge Univ. Press.

Tenner, T. J., M. M. Hirschmann, A. C. Withers, and R. L. Hervig (2009), Hydrogen partitioning between nominally anhydrous upper mantle minerals and melt between 3 and 5 GPa and applications to hydrous peridotite partial melting, *Chem. Geol.*, *262*(1–2), 42–56.

Tenner, T. J., M. M. Hirschmann, A. C. Withers, and P. Ardia (2012), H_2O storage capacity of olivine and low-Ca pyroxene from 10 to 13 GPa: Consequences for dehydration melting above the transition zone, *Contrib. Mineral. Petrol.*, *163*(2), 297–316, doi:10.1007/s00410-011-0675-7.

Toplis, M. J. (2005), The thermodynamics of iron and magnesium partitioning between olivine and liquid: Criteria for assessing and predicting equilibrium in natural and experimental systems, *Contrib. Mineral. Petrol.*, *149*(1), 22–39.

van Kan Parker, M., A. Liebscher, D. Frei, J. van Sijl, W. van Westrenen, J. Blundy, and G. Franz (2010), Experimental and computational study of trace element distribution between orthopyroxene and anhydrous silicate melt: Substitution mechanisms and the effect of iron, *Contrib. Mineral. Petrol.*, *159*(4), 459–473, doi:10.1007/s00410-009-0435-0.

van Westrenen, W., J. D. Blundy, and B. J. Wood (2001), High field strength element/rare earth element fractionation during partial melting in the presence of garnet: Implications for identification of mantle heterogeneities, *Geochem. Geophys. Geosyst.*, *2*(7), 1039, doi:10.1029/2000GC000133.

Wang, W., and E. Takahashi (2000), Subsolidus and melting experiments of K-doped peridotite KLB-1 to 27 GPa: Its geophysical and geochemical implications, *J. Geophys. Res.*, *105*(B2), 2855–2868, doi:10.1029/1999JB900366.

Wänke, H., and G. Dreibus (1994), Chemistry and accretion history of Mars, *Philos. Trans. R. Soc.*, *A 349*, 285–293.

Watters, W. A., M. T. Zuber, and B. H. Hager (2009), Thermal perturbations caused by large impacts and consequences for mantle convection, *J. Geophys. Res.*, *114*, E02001, doi:10.1029/2007JE002964.

Werner, S. C. (2008), The early Martian evolution—Constraints from basin formation ages, *Icarus*, *195*(1), 45–60, doi:10.1016/j.icarus.2007.12.008.

Werner, S. C., and B. A. Ivanov (2015), Exogenic dynamics, cratering, and surface ages, in *Physics of Terrestrial Planets and Moons, Treatise on Geophys.*, vol. 10, 2nd ed., edited by T. Spohn, chap. 10.10, pp. 327–365, Elsevier, Amsterdam, doi:10.1016/B978-0-444-53802-4.00170-6.

Wieczorek, M. A. (2008), Constraints on the composition of the Martian south polar cap from gravity and topography, *Icarus*, *196*(2), 506–517, doi:10.1016/j.icarus.2007.10.026.

Wieczorek, M. A., and M. T. Zuber (2004), Thickness of the Martian crust: Improved constraints from geoid-to-topography ratios, *J. Geophys. Res.*, *109*, E01009, doi:10.1029/2003JE002153.

Williams, J.-P., and F. Nimmo (2004), Thermal evolution of the Martian core: Implications for an early dynamo, *Geology*, *32*(2), 97–100.
Wood, B. J., and J. D. Blundy (2002), The effect of H_2O on crystal-melt partitioning of trace elements, *Geochim. Cosmochim. Acta*, *66*(20), 3647–3656.
Wood, B. J., and J. D. Blundy (2014), Trace element partitioning: The influences of ionic radius, cation charge, pressure, and temperature, in *The Mantle and Core, Treatise on Geochemistry*, vol. 3, 2nd ed., edited by R. W. Carlson, chap. 3.11, pp. 421–448, Elsevier, Amsterdam, doi:10.1016/B978-0-08-095975-7.00209-6.
Wood, B. J., J. D. Blundy, and J. A. C. Robinson (1999), The role of clinopyroxene in generating U-series disequilibrium during mantle melting, *Geochim. Cosmochim. Acta*, *63*(10), 1613–1620.
Zhao, Y., M. E. Zimmerman, and D. L. Kohlstedt (2009), Effect of iron content on the creep behavior of olivine: 1. Anhydrous conditions, *Earth Planet. Sci. Lett.*, *287*(1–2), 229–240, doi:10.1016/j.epsl.2009.08.006.
Zuber, M. T., et al. (2000), Internal structure and early thermal evolution of Mars from Mars Global Surveyor topography and gravity, *Science*, *287*(5459), 1788–1793, doi:10.1126/science.287.5459.1788.

Journal of Geophysical Research – Planets

Supporting Information for

On the relative importance of thermal and chemical buoyancy in regular and impact-induced melting in a Mars-like planet

Thomas Ruedas[1,2] and Doris Breuer[2]

[1] Institute of Planetology, Westfälische Wilhelms-Universität Münster, Germany

[2] Institute of Planetary Research, German Aerospace Center (DLR), Berlin, Germany

Contents of this file

Additional Supporting Information (Files uploaded separately)

1. Datasets displayed in Figures 2, 3, 4, 6, 7, 8, and A.1 of the main text: `f.dat`, `I-36-T_f.dat`, `I-36-T_T.dat`, `I-36-TC_f.dat`, `I-36-TC_T.dat`, `marssol.dat`, `qs_t.dat`, `Raeff10_t.dat`, `Ref-36-TC_T.dat`, `rho.dat`, `U-36-T_T.dat`, `U-36-TC_T.dat`, `vB.dat`, `zle_t.dat`
2. Animation of Model I-36/TC (`I-36_TC.mp4`)
3. Animation of Model I-36/T (`I-36_T.mp4`)

1 Thermoelastic model

The starting point for the calculation of the thermoelastic properties of the solid silicate part of the planet is the set of mineral endmember properties, which we assume to form ideal solid solutions. We have collected a large number of experimental data for many endmembers of the most common (basaltic) crust and mantle minerals and fitted them to the third-order Birch–Murnaghan equation of state and to the Mie–Grüneisen–Debye equation of state in order to determine the key properties, which are listed in Table 1. Possible effects of water on these properties have been neglected at this point, because the water concentrations of the models in this paper are generally rather low, and for many minerals water-related effects are poorly known. Some hypothetical endmembers that are needed for the purpose of calculation but do not actually exist have also been included; their properties were inferred from systematics, as were properties of phases for which no or insufficient data were available.

Theoretical framework The thermoelastic properties of the mineral endmembers are formulated in the framework of quasi-harmonic theory. In the harmonic approximation, the internal energy of a crystal at temperature T is split into a "cold" contribution that accounts for the static pressure and compression and a vibrational thermal part (*Grüneisen*, 1912):

$$E = E_\mathrm{c} + E_\mathrm{vib} = E_\mathrm{c} + \sum_{i=1}^{3N} \hbar\omega_i \left(\frac{1}{2} + \frac{1}{\exp\left(\frac{\hbar\omega_i}{k_\mathrm{B}T}\right) - 1} \right), \tag{1}$$

where the sum is taken over the $3N$ modes ω_i of an N-oscillator crystal (e.g., *Ashcroft and Mermin*, 1976). A similar additive representation also holds for the Helmholtz potential F, from which all thermodynamic properties can be derived. The cold compressional contribution at pressure p to the Helmholtz potential depends on the choice of equation of state; we use the third-order Birch–Murnaghan equation of state,

$$p = \frac{3}{2} K_{T0} \left[\left(\frac{V_0}{V}\right)^{\frac{7}{3}} - \left(\frac{V_0}{V}\right)^{\frac{5}{3}} \right] \left\{ 1 + \frac{3}{4}(K'_{T0} - 4) \left[\left(\frac{V_0}{V}\right)^{\frac{2}{3}} - 1 \right] \right\}, \tag{2}$$

which has been the most popular choice in the literature for decades; V, K_T, and K'_T are the molar volume, the isothermal bulk modulus, and its pressure derivative, respectively, and the subscript 0 indicates the value at standard pressure.

The thermal contributions are described by Mie–Grüneisen–Debye theory. The Debye model of phonons (*Debye*, 1912) introduces a simplified description of the phonon spectrum based on a parabolic density of states that is cut off at a characteristic frequency ω_D, corresponding to a temperature $\theta_\mathrm{D} = \hbar\omega_\mathrm{D}/k_\mathrm{B}$, the Debye temperature; $\hbar$ and k_B are Planck's and Boltzmann's constants, respectively (the former divided by 2π). With this simplification, the vibrational energy becomes

$$E_\mathrm{vib} = 9NRT \left(\frac{T}{\theta_\mathrm{D}}\right)^3 \int_0^{\frac{\theta_\mathrm{D}}{T}} \frac{t^3}{\exp t - 1}\,\mathrm{d}t = 3NRT\mathcal{D}_3\left(\frac{\theta_\mathrm{D}}{T}\right), \tag{3}$$

i.e., it approaches $3NRT$ at $T \gg \theta_\mathrm{D}$, and with $F = E - TS$ the Helmholtz free energy becomes

$$F_\mathrm{vib} = 9NRT \left(\frac{T}{\theta_\mathrm{D}}\right)^3 \int_0^{\frac{\theta_\mathrm{D}}{T}} \ln(1 - \exp(-t))\, t^2\,\mathrm{d}t; \tag{4}$$

$\mathcal{D}_3$ in eq. 3 is the Debye function of order 3. The characteristic temperature is assumed to depend explicitly only on volume (*Grüneisen*, 1926) in a manner described by the thermal Grüneisen parameter

$$\gamma = \gamma_0 \left(\frac{V}{V_0}\right)^q \tag{5a}$$

$$\theta_\mathrm{D} = \theta_{\mathrm{D}0} \exp\left(\frac{\gamma_0 - \gamma}{q}\right) = \theta_{\mathrm{D}0} \exp\left\{\frac{\gamma_0}{q}\left[1 - \left(\frac{V}{V_0}\right)^q\right]\right\}; \tag{5b}$$

the parameter q is often close to 1 (e.g., *Stixrude and Bukowinski*, 1990). The second

temperature derivative of F_{vib} yields the isochoric heat capacity,

$$c_V = -T\left(\frac{\partial^2 F}{\partial T^2}\right)_V = 9NR\left(\frac{T}{\theta_\mathrm{D}}\right)^3 \int_0^{\frac{\theta_\mathrm{D}}{T}} \frac{t^4 \exp t}{(\exp t - 1)^2}\,\mathrm{d}t = 9NR\left(\frac{T}{\theta_\mathrm{D}}\right)^3 \int_0^{\frac{\theta_\mathrm{D}}{T}} t^2 \mathcal{E}_2(t)\,\mathrm{d}t, \quad (6)$$

where $\mathcal{E}_2(t)$ is the Einstein function of order 2. The volume derivative of F_{vib} gives the thermal pressure,

$$p_{\mathrm{th}} = \frac{\gamma}{V}\left(E_{\mathrm{vib}}(V,T) - E_{\mathrm{vib}}(V,T_0)\right), \quad (7)$$

and the thermal contribution to the isothermal bulk modulus,

$$K_{T,\mathrm{th}} = \frac{\gamma}{V}\left[(\gamma + 1 - q)\left(E_{\mathrm{vib}}(V,T) - E_{\mathrm{vib}}(V,T_0)\right) - \gamma\left(Tc_V(V,T) - T_0 c_V(V,T_0)\right)\right] \quad (8)$$

(e.g., *Ita and Stixrude*, 1992). The thermal expansivity, the adiabatic bulk modulus, and the isobaric heat capacity are then given by the standard thermodynamic relations

$$\alpha = \frac{\gamma c_V}{K_T V} \quad (9)$$

$$K_S = \frac{c_p}{c_V} K_T = K_T(1 + \gamma\alpha T) \quad (10)$$

$$c_p = c_V(1 + \gamma\alpha T) = c_V\left(1 + \frac{\gamma^2 T c_V}{K_T V}\right). \quad (11)$$

As closed-form solutions of the integrals in eqs. 3, 4, and 6 are not available, approximate solutions based on summation formulae are used. The integral in the expression for the vibrational energy (eq. 3) can be expressed as

$$\int_0^{\frac{\theta_\mathrm{D}}{T}} \frac{t^3}{\exp t - 1}\,\mathrm{d}t = \begin{cases} \left(\frac{\theta_\mathrm{D}}{T}\right)^3 \left[\frac{1}{3} - \frac{1}{8}\frac{\theta_\mathrm{D}}{T} + \sum_{k=1}^{\infty} \frac{B_{2k}}{(2k+3)(2k)!}\left(\frac{\theta_\mathrm{D}}{T}\right)^{2k}\right] & \frac{\theta_\mathrm{D}}{T} \lesssim 0.5 \\ 6\zeta(4) - \sum_{k=1}^{\infty} \exp\left(-k\frac{\theta_\mathrm{D}}{T}\right)\left[\frac{1}{k}\left(\frac{\theta_\mathrm{D}}{T}\right)^3 + \frac{3}{k^2}\left(\frac{\theta_\mathrm{D}}{T}\right)^2 + \frac{6}{k^3}\left(\frac{\theta_\mathrm{D}}{T}\right) + \frac{6}{k^4}\right] & \text{else,} \end{cases} \quad (12)$$

where B_{2k} are the Bernoulli numbers and ζ is the Riemann zeta function (*Abramowitz and Stegun*, 1964, eqs. 27.1.1–3 with $n = 3$).

The integral in the expression for the specific heat (eq. 6) belongs to a class of functions that are definite integrals of the Einstein functions of order s,

$$I_n(s, x_\mathrm{D}) = \int_0^{x_\mathrm{D}} \frac{x^n \exp x}{(\exp x - 1)^s}\,\mathrm{d}x = \int_0^{x_\mathrm{D}} x^{n-s}\mathcal{E}_s(x)\,\mathrm{d}x, \quad (13)$$

for which *Mamedov et al.* (2009) have derived the summation formula

$$I_n(s, x_\mathrm{D}) = \sum_{m=0}^{\infty} (-1)^m \binom{-s}{m} H_{nm}(s, x_\mathrm{D}) \quad (14)$$

with

$$H_{nm}(s, x_\mathrm{D}) = \frac{n!}{(m+s-1)^{n+1}}\left\{1 - \exp[-x_\mathrm{D}(m+s-1)]\sum_{k=0}^{n}\frac{[x_\mathrm{D}(m+s-1)]^k}{k!}\right\}. \quad (14a)$$

Using

$$\binom{-s}{m} = (-1)^m \binom{s+m-1}{m} = (-1)^m \frac{(s+m-1)!}{m!(s-1)!} \tag{14b}$$

and setting $n = 4$ and $s = 2$ as in eq. 6, eq. 14 can be simplified to

$$I_4(2, x_\mathrm{D}) = \sum_{m=0}^{\infty} (m+1) H_{4m}(2, x_\mathrm{D}). \tag{14c}$$

The integrals for the vibrational Helmholtz potential and its temperature derivative, the entropy S, can be expressed with similar formulas using partial integration if desired.

Estimates of unconstrained parameters In some cases, there are no data for a given endmember, for instance if that endmember is not thermodynamically stable and hence hypothetical, as is the case with Fe-wadsleyite, or if there are simply no experimental data. In such cases, the parameters have to be estimated using available data for similar minerals. In order to estimate the molar volume, we consider the ratios of known V_0 of minerals with similar structure or composition; for instance, the molar volume of Fe-wadsleyite is estimated from Mg-wadsleyite, ringwoodite, and ahrensite assuming that

$$\frac{V_{0,\mathrm{Fewa}}}{V_{0,\mathrm{Mgwa}}} = \frac{V_{0,\mathrm{ah}}}{V_{0,\mathrm{ri}}}. \tag{15}$$

For estimates of the bulk modulus, we use the empirical relation

$$MV = const. \Leftrightarrow MV = M_\mathrm{ref} V_\mathrm{ref} \tag{16}$$

(e.g., *Duffy and Anderson*, 1989), where M is an elastic modulus. The p derivative is unfortunately not well captured by any empirical relation, but differentiating with $M = K_T$ yields

$$K'_T = (K'_{T\mathrm{ref}} - 1)\frac{V_\mathrm{ref}}{V} + 1; \tag{17}$$

it generally does not show very large variation. The thermal parameters could be estimated based on the assumption that volume is the only factor that affects γ and q so that the Grüneisen parameter could be estimated using eq. 5a with γ_0 and V_0 from the known substance and V for the unknown substance, i.e.,

$$\gamma = \gamma_\mathrm{ref} \left(\frac{V}{V_\mathrm{ref}}\right)^{q_\mathrm{ref}}, \tag{18}$$

with $q = q_\mathrm{ref}$, as q would be poorly constrained by any available data. We emphasize that this is an ad hoc ansatz, and we will investigate in more detail below how well it works.

To determine θ_D, we first consider the (elastic) Debye temperature:

$$\theta_\mathrm{D} = \frac{h}{k_\mathrm{B}} \left(\frac{3NN_\mathrm{A}}{4\pi V}\right)^{\frac{1}{3}} v_\mathrm{D} = \frac{h}{k_\mathrm{B}} \left(\frac{9NN_\mathrm{A}}{4\pi V \left(\frac{1}{v_\mathrm{P}^3} + \frac{2}{v_\mathrm{S}^3}\right)}\right)^{\frac{1}{3}} = \frac{h}{k_\mathrm{B}} \left(\frac{9NN_\mathrm{A}}{4\pi V \left[2 + \left(\frac{v_\mathrm{S}}{v_\mathrm{P}}\right)^3\right]}\right)^{\frac{1}{3}} v_\mathrm{S} \tag{19a}$$

(*Poirier*, 2000, eq. 3.36), where v_D, v_P, and v_S are the Debye, compressional, and shear velocity, respectively. Assuming that the mineral is a Cauchy solid ($v_\mathrm{P} = \sqrt{3}v_\mathrm{S}$), the results of the parameters already determined for the cold compression can be used together with

$$v_\mathrm{D} = \sqrt{\frac{3K_\mathrm{S}}{5\varrho}} \left(\frac{3}{2 + \left(\frac{1}{3}\right)^{\frac{3}{2}}} \right)^{\frac{1}{3}} \approx 0.86 \sqrt{\frac{K_S}{\varrho}} \approx \sqrt{\frac{K_T V}{m_\mathrm{mol}}}. \tag{19b}$$

to deduce the unknown Debye temperature:

$$\frac{\theta_\mathrm{D}}{\theta_\mathrm{D,ref}} = \left(\frac{N}{N_\mathrm{ref}} \right)^{\frac{1}{3}} \left(\frac{K_T m_\mathrm{mol,ref}}{K_{T,\mathrm{ref}} m_\mathrm{mol}} \right)^{\frac{1}{2}} \left(\frac{V}{V_\mathrm{ref}} \right)^{\frac{1}{6}}; \tag{19c}$$

often one will choose the reference mineral so that $N = N_\mathrm{ref}$.

In order to assess the quality of such estimates and test what sort of analogue materials are suitable for applying such systematics, we can make such systematic comparisons for endmembers for which there are actual measurements to compare with; the data are taken from the database of which Table 1 shows a subset. The plots in Fig. 1 show predicted vs. measured values for several materials, grouped by mineral structure and composition. The groups are Olivine (forsterite and fayalite), Orthopyroxene (orthoenstatite and orthoferrosilite), Clinopyroxene (2–2) (clinopyroxenes with one of the bivalent cations Mg^{2+}, Fe^{2+}, and Ca^{2+} on each of the M1 and M2 sites), Clinopyroxene (1–3) (clinopyroxenes with Na^{+} as the monovalent cation and one of the trivalent cations Al^{3+}, Fe^{3+}, and Cr^{3+} on the M1 and M2 sites), Al–Cr spinel (Spinels with Mg^{2+} or Fe^{2+} as the bivalent ion and Al^{3+} or Cr^{3+} as the trivalent ion), Si spinelloid (the high-p polymorphs of olivine, i.e., Mg-wadsleyite, ringwoodite, ahrensite), Al–Cr–Fe garnet (the various garnets with the bivalent cations Mg^{2+}, Fe^{2+}, or Ca^{2+} on the X site and the trivalent cations Al^{3+}, Fe^{3+}, and Cr^{3+} on the Y site), Mg–Al/Si garnet (pyrope and Mg-majorite), Ilmenite (Mg-akimotoite, corundum, eskolaite), Oxide (periclase and wüstite), and Perovskite/postperovskite (bridgmanite, Ca-perovskite, Mg-postperovskite).

In order to estimate an unknown V_0 from similar minerals, three reference materials are needed according to eq. 15, which limits the number of data available for testing. For the three mineral groups for which there are sufficient data, the estimates are very accurate (Figure 1a).

For the other parameters, only one reference mineral is required. In Figures 1b–e, data are shown for two sets of calculations. In the first one, which is plotted with solid symbols, only the target parameter is assumed to be unknown but the other properties, especially V_0 are derived from experiments. In the other one, which is plotted with open symbols, all properties of the target materials are assumed to be unknown, i.e., V_0, K_{T0}, K'_{T0}, γ_0, q, and θ_D are derived from systematics, implying that errors propagate through the steps of the calculation. In most calculations, especially those of the first set, we chose the reference material so that it differs from the target material only in one type of ions. For some mineral groups, we also considered reference materials differing by two types of ions or having a slightly different crystal structure (Si spinelloid, Perovskite/postperovskite); this subset is plotted in a paler hue of the same color.

The estimates for K_{T0} indicate that eq. 16 works quite well for several mineral groups, even if the reference mineral differs by more than a single ion (Figure 1b). The reliability of the formula deteriorates towards materials with higher K_{T0}, which are typical for higher-pressure phases. Unfortunately, the performance does not generally remain at that level

for K'_{T0} (Figure 1c). The reason is at least in some cases that the K'_{T0} values of the reference materials are themselves not very well constrained. The estimates for γ_0 and θ_D are satisfactory in many cases (Figure 1d,e), but it is probably always safer to make several estimates with different minerals if possible, and to observe whether they cluster around certain values.

Database assembly and fitting procedure The thermodynamical calculations are based on a large set of experimental data for the endmembers. The database was assembled according to the following principles:

- It was tried to use observables that can be measured as directly as possible, i.e., without intermediate steps or additional assumptions or data. Specifically, this restricts the data to direct measurements of volume V (or rather the lattice parameter) as a function of p and/or T, e.g. by X-ray crystallography, and calorimetric measurements that yield c_p or the differential enthalpy $\Delta H = H(T) - H(T_{\mathrm{ref}})$. Density measurements from immersion (Archimedean) experiments were admitted if they agreed reasonably well with the other STP data and/or the sample had a very low ($\ll 1\%$) porosity; however, if X-ray densities were available for the same sample, the X-ray density is preferred.

- In addition to the STP measurements from compression or expansion studies, an effort was made to include many additional measurements conducted independently only at standard conditions, e.g., for structure refinement. The purpose is to constrain the reference volumes V_0 as tightly as possible rather than treating it as a freely adjustable parameter in the cold compression fit, because that would give the low-T, high-p data an influence on V_0 but not the low-p, high-T data, which does not seem to be justified.

- Results from shock experiments are not admitted, because the temperature is usually poorly constrained.

- Results from ab-initio, molecular dynamics, or similar numerical calculations are not admitted.

- If possible, only data from chemically pure endmember samples were used, whereby "pure" is defined as "containing less than 1 mol% components that are not part of the ideal endmember composition". Only if pure samples were not available, samples with more impurities were also taken into consideration.

- Frequently, the temperature at which isothermal compression experiments are conducted is only specified as "room temperature", or no information is given about the temperature at all. In such cases, the experiments are assumed to have been carried out at "room temperature", which is assumed to be 298.15 K (25°C).

- Some fits were restricted if necessary due to poor convergence. Most importantly, K'_{T0} was never allowed to be smaller than 5/3 in order to enforce a thermodynamic condition for $p \to \infty$ (e.g., *Stacey and Davis*, 2004), nor was it allowed to exceed 9. We emphasize that calculations at high p for minerals in which the fit gave such extreme values should be done with particular care if they cannot be avoided.

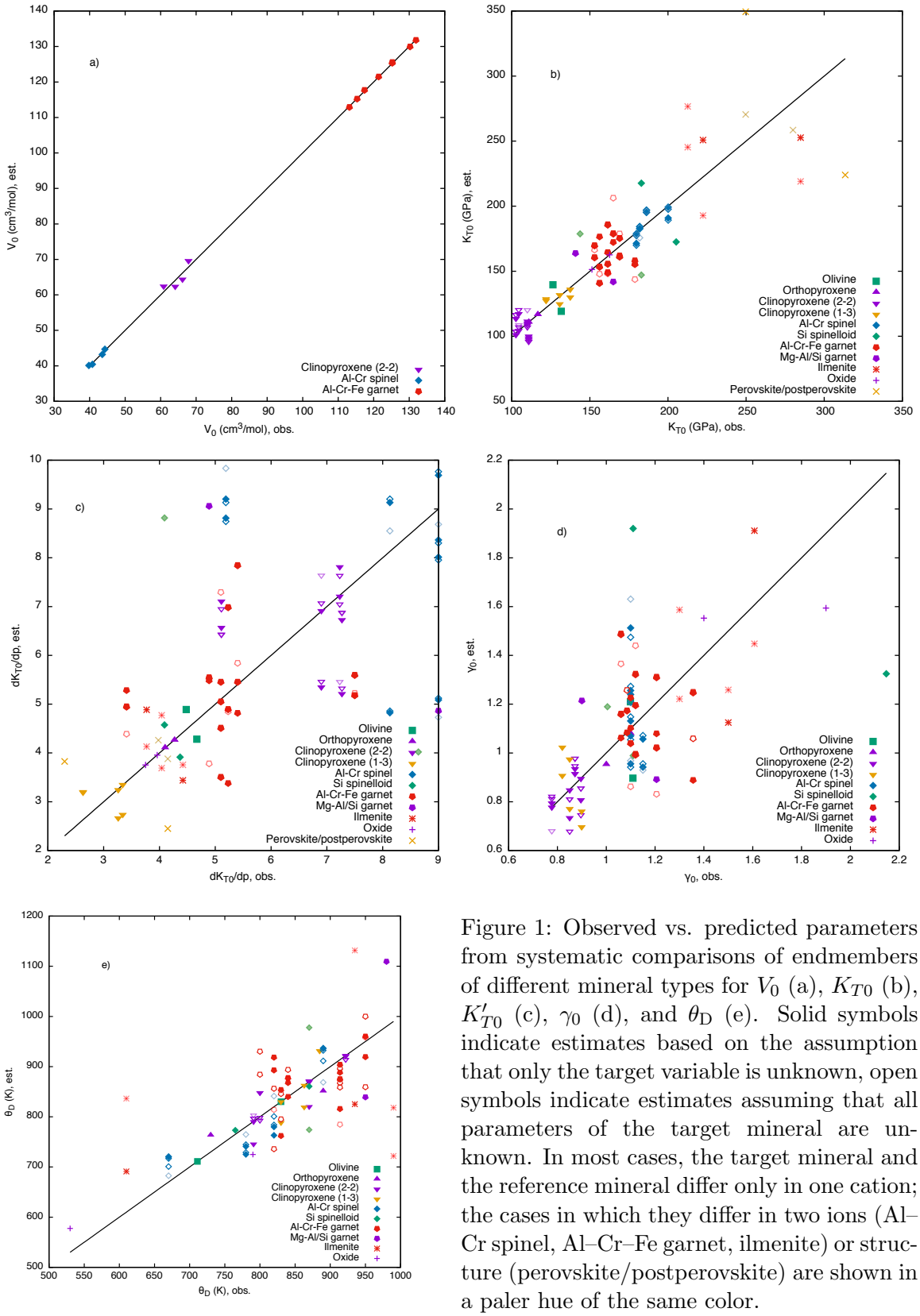

Figure 1: Observed vs. predicted parameters from systematic comparisons of endmembers of different mineral types for V_0 (a), K_{T0} (b), K'_{T0} (c), γ_0 (d), and θ_{D} (e). Solid symbols indicate estimates based on the assumption that only the target variable is unknown, open symbols indicate estimates assuming that all parameters of the target mineral are unknown. In most cases, the target mineral and the reference mineral differ only in one cation; the cases in which they differ in two ions (Al–Cr spinel, Al–Cr–Fe garnet, ilmenite) or structure (perovskite/postperovskite) are shown in a paler hue of the same color.

- Data from tabulated, "smoothed" datasets such as the data tables by *Robie et al.* (1978) or *Robie and Hemingway* (1995) are avoided, because the fitting model necessarily introduces a certain bias towards that model.

- If possible, original data were taken from tables in the respective publication. In numerous cases, however, authors did not tabulate their data but provided only plots. In this case, the data points were taken from a digital version of the plot with a dedicated tool trying to preserve the highest accuracy permitted by the quality of the plot. We expect the accuracy of these readings to be generally better than experimental error, especially in compression experiments.

- Only data from 1950 or later are admitted.

The final material parameters are determined in several steps:

1. If volume measurements at standard conditions were available, V_0 was determined as the arithmetic mean of all accepted V_0 values and kept fixed afterwards.

2. The room-temperature compression data are fitted to the isothermal equation of state with a Levenberg–Marquardt algorithm in order to determine K_{T0} and K'_{T0}.

3. If differential enthalpy measurements are available, each such dataset is recalculated into a heat capacity dataset individually. In the literature, it is common to give a mean isobaric specific heat by a finite difference form of its relation with the enthalpy,

$$c_p = \left(\frac{\partial H}{\partial T}\right)_p \Rightarrow c_{p,\mathrm{mean}} = \frac{H(T) - H(T_{\mathrm{ref}})}{T - T_{\mathrm{ref}}}, \tag{20}$$

   giving a mean specific heat; the actual c_p dependence is often cast in the form of empirical polynomial formulae whose coefficients are determined by integration and fitting to the ΔH data. As we do not use such formulae, we chose to approximate the actual $c_p(T)$ by

$$\frac{\Delta H_2 - \Delta H_1}{T_2 - T_1} = \frac{H_2 - H_1}{T_2 - T_1} \approx \left(\frac{\partial H}{\partial T}\right)_p = c_p \tag{21}$$

   or indeed by more accurate higher-order finite-difference expressions (e.g., *Fornberg*, 1998); note that the expressions must be suitable for unequally spaced samples, because experimental data are often not equally spaced so that the familiar FD operators for equispaced grids cannot be used. This method is found to yield satisfactory results if the dataset is of sufficiently high quality.

4. A Simulated Annealing algorithm is used to fit the standard-pressure datasets of volumetric expansion, thermal equation of state, and isobaric heat capacity separately and together.

5. All fits as well as all curves derived from systematics are controlled visually, and parameters are adjusted by trial and error if necessary, often with the aid of systematics. In the case of the isothermal fits, this was not usually necessary, but the thermal fits frequently required such adjustments because the results of the fitting procedure did not produce physically acceptable matches to all available data. The adjustments had the goal to approximate all datasets as well as possible visually and physically; in particular,

- volumetric expansion should be a monotonically increasing function whose slope approaches zero for $T \to 0$;
- isobaric heat capacity should be a non-decreasing function if possible at all, or at least show only a minimal decline at $T \gg \theta_{\mathrm{D}}$.

Especially the c_p datasets frequently make the thermal fits difficult, because often θ_{D} is not, or only barely, reached, and the data are insufficient for θ_{D} to be found properly by the fitting algorithm; as a result, the algorithms would often find too small values. Volumetric expansion is fairly insensitive towards the choice of θ_{D} and does not seem very useful to constrain this parameter.

The thermoelastic parameters determined by this approach that we used in our modeling study are summarized in Table 1, but we emphasize that this compilation and the fits are continually improved as new data become available and that we hope to remove shortcomings of the current fit in the future.

Properties of the bulk rock In order to determine the properties of the bulk mantle material from the endmember properties, two more steps have to be completed, namely the calculation of the properties of the solid solution minerals that represent the individual mineral phases and the derivation of the properties of the composite formed by them.

For the solid solution properties we follow the practice of many previous authors to assume ideal solid solution of endmembers, which often is a fairly good approximation and accurate enough for our purposes. Ideal mixing implies that the molar volume of the solid solution, V_{ss}, is the linear combination of the molar volumes of the endmembers, V_i, with the weights given by their respective molar fractions $\underline{X}_i$ as determined from bulk chemistry and, if melting has occurred, with the help of the partitioning coefficients described in more detail in Section 3. The density of the solid solution is calculated from V_{ss} and the mole-weighted average of the end-member molecular masses, and the thermal expansion coefficient and the isothermal and adiabatic bulk moduli then follow from their thermodynamic definitions:

$$\alpha_{\mathrm{ss}} = \frac{1}{\sum \underline{X}_i V_i} \left(\frac{\partial}{\partial T}\right)_p \left(\sum \underline{X}_i V_i\right) = \frac{\sum \underline{X}_i V_i \alpha_i}{V_{\mathrm{ss}}}, \tag{22}$$

$$K_{T,S\mathrm{ss}} = \left[\frac{1}{\sum \underline{X}_i V_i} \left(\frac{\partial}{\partial p}\right)_{T,S} \left(\sum \underline{X}_i V_i\right)\right]^{-1} = \frac{V_{\mathrm{ss}}}{\sum \frac{\underline{X}_i V_i}{K_{T,Si}}}, . \tag{23}$$

Assuming complete relaxation, which should be applicable to long-duration processes in planetary interiors, the expansivity and bulk moduli of the composite material are then estimated as isostress (Reuss) averages of the properties of the component minerals (e.g., *Stacey*, 1998):

$$\alpha^{\mathrm{R}}_{\mathrm{mc}} = \frac{1}{m_{\mathrm{mol}} \sum X_i \frac{V_i}{m_{\mathrm{mol}_i}}} \left(\frac{\partial}{\partial T}\right)_p \left(m_{\mathrm{mol}} \sum X_i \frac{V_i}{m_{\mathrm{mol}_i}}\right) = \varrho_{\mathrm{mc}} \sum \frac{X_i}{\varrho_i} \alpha_i = \sum \tilde{X}_i \alpha_i \tag{24}$$

$$K^{\mathrm{R}}_{\mathrm{mc}} = \frac{1}{\varrho_{\mathrm{mc}} \sum \frac{X_i}{\varrho_i K_i}} = \frac{1}{\sum \frac{\tilde{X}_i}{K_i}}, \tag{25}$$

where X_i and $\tilde{X}_i$ are the mass and volume fractions of the constituents, respectively. For the calculation of seismic velocities, it is not appropriate to assume relaxation, however. One

Table 1: Thermoelastic parameters of mineral endmembers for the third-order Birch–Murnaghan and Mie–Grüneisen–Debye equations of state. Properties inferred from systematics, in particular of hypothetical phases, are italicized.

Endmember	Formula	f.u.p.c.	V_0 (cm^3/mol)	K_{T0} (GPa)	K'_T	γ_0	q	θ_D (K)
Forsterite	Mg_2SiO_4	4	43.6639	126.36	4.48	1.109	1.5	830
Fayalite	Fe_2SiO_4	4	46.2735	134.41	4.08	1.1	4.2	711
Mg-wadsleyite	Mg_2SiO_4	8	40.532	143.74	8.64	1.005	0.7	870
Fe-wadsleyite	Fe_2SiO_4	8	*42.89*	*135.8*	*8.22*	*1.045*	*0.7*	*709*
Ringwoodite	Mg_2SiO_4	8	39.6095	182.93	4.09	1.11	3	870
Ahrensite	Fe_2SiO_4	8	42.0109	205.23	4.37	2.147	1.9	765
Orthoenstatite	$Mg_2Si_2O_6$	8	62.6287	116.72	4.27	1	1.5	890
Orthoferrosilite	$Fe_2Si_2O_6$	8	65.9217	*110.89*	*4.1*	1.1	2.8	730
High-p clinoenstatite	$Mg_2Si_2O_6$	4	60.8544	110	7.23	0.777	1.7	922
High-p clinoferrosilite	$Fe_2Si_2O_6$	4	*64.087*	*104.45*	*6.9*	*0.85*	*1.3*	*791*
Diopside	$CaMgSi_2O_6$	4	66.1434	102.67	7.27	0.896	1.7	870
Hedenbergite	$CaFeSi_2O_6$	4	67.8477	110.85	5.11	0.872	3	800
Jadeite	$NaAlSi_2O_6$	4	60.5346	137.41	3.34	0.899	2	885
Anorthite	$CaAl_2Si_2O_8$	8	100.8501	75.84	1.67	0.4	2.5	900
High albite	$NaAlSi_3O_8$	4	100.3872	57.27	3.16	0.566	2.5	950
Spinel	$MgAl_2O_4$	8	39.7691	200.29	5.18	1.12	3	880
Hercynite	$FeAl_2O_4$	8	40.7787	186.19	9	1.1	1.6	820
Magnesiochromite	$MgCr_2O_4$	8	43.5834	179.97	8.37	1.1	1.7	780
Chromite	$FeCr_2O_4$	8	44.2849	181.44	9	1.1	1.7	670
Mg-Ca-ferrite	$MgAl_2O_4$	6	36.1357	219.64	3.22	1.662	1.06	980
Fe-Ca-ferrite	$FeAl_2O_4$	6	*37.052*	*214.21*	*3.17*	*1.42*	*1.06*	*879*
Na-Ca-ferrite	$NaAlSiO_4$	6	36.2951	185.4	4.63	0.8	3	1000
Pyrope	$Mg_3Al_2Si_3O_{12}$	8	113.1768	165.11	4.88	1.206	0.9	950
Almandine	$Fe_3Al_2Si_3O_{12}$	8	115.3381	169.01	5.4	1.1	1	840
Grossular	$Ca_3Al_2Si_3O_{12}$	8	125.2401	161.44	5.1	1.12	0.9	914
Uvarovite	$Ca_3Cr_2Si_3O_{12}$	8	130.2582	178.8	3.41	1.06	1.7	820
Mg-majorite	$MgSiO_3$	32	28.5049	140.84	9	0.9	1.3	980
Fe-majorite	$FeSiO_3$	32	*29.05*	*138.2*	*8.85*	*0.92*	*1.3*	*850*
Ca-majorite	$CaSiO_3$	32	*31.54*	*127.27*	*8.23*	*1.03*	*1.3*	*881*
Na-majorite	$Na_2MgSi_5O_{12}$	8	111.0995	178.35	4.85	1.179	0.96	1145
Mg-akimotoite	$MgSiO_3$	6	26.343	212.62	4.04	1.3	1.1	990
Fe-akimotoite	$FeSiO_3$	6	*27.74*	*201.89*	*3.89*	*1.38*	*1.2*	*883*
Corundum	Al_2O_3	6	25.5761	284.92	3.77	1.5	1.9	935
Eskolaite	Cr_2O_3	6	29.0546	222.42	4.42	1.607	2.8	610
α-quartz	SiO_2	3	22.6854	39.53	4.96	0.67	3.5	900
β-quartz	SiO_2	3	23.7	*39.53*	*4.96*	0	1	1100
Coesite	SiO_2	16	20.5772	99.79	3.63	0.35	2.3	980
Stishovite	SiO_2	2	14.0176	304.6	4.25	1.4	1.4	1120
NAL phase	$NaMgAl_3SiO_8$	2	55.0267	190.62	4.31	0.87	2.67	890
CAS phase	$CaAl_4Si_2O_{11}$	2	97.6683	155.93	7.41	1.2	1.07	1015

approach is to determine also the isostrain (Voigt) average of the adiabatic bulk moduli of the constituent minerals,

$$K_\mathrm{mc}^\mathrm{V} = \varrho_\mathrm{mc} \sum \frac{X_i}{\varrho_i} K_i = \sum \tilde{X}_i K_i, \tag{26}$$

and to compute the effective composite modulus as the arithmetic mean of the Reuss and Voigt bound (Voigt–Reuss–Hill average); the bulk rock density is determined from the densities of the constituent minerals:

$$\varrho_\mathrm{mc} = \left(\sum \frac{X_i}{\varrho_i} \right)^{-1} = \sum \tilde{X}_i \varrho_i. \tag{27}$$

There are tighter bounds, such as the Hashin–Shtrikman bounds, but for the time being, we use the VRH average for the calculation of the bulk sound velocity.

The thermal conductivity k is linked to some extent to the thermoelastic properties and was also calculated in two steps. k and the thermal diffusivity $\kappa = k/(\varrho c_p)$ were determined for each (solid-solution) mineral phase individually using a representation of the temperature and composition dependence based on the κ parameterizations from *Hofmeister and Branlund* (2015) for the phonon contribution and adding the (relatively unimportant) pressure-independent radiative component as given by *Hofmeister* (1999). The pressure dependence of the phononic part of k and κ is not well constrained experimentally, and it was assumed here that $k(p)$ scales with the bulk modulus (e.g., *Hofmeister and Branlund*, 2015). The conductivity of the bulk material was taken to be the mean of the generalized Hashin–Shtrikman bounds for a composite of the individual minerals (*Berryman*, 1995).

Near the surface, the material is generally assumed to have a certain porosity. We keep the approach already used by *Ruedas et al.* (2013a) to adopt a description by *Leone et al.* (2011) based on work by *Head and Wilson* (1992), which provides pressure-dependent formulae for the density and thermal conductivity of porous materials:

$$\varrho(p) = \varrho_{\mathrm{solid}}(1-\varphi), \tag{28}$$

$$k(p) = k_{\mathrm{solid}}(1 - 1.738\varphi + 0.8228\varphi^2), \tag{29}$$

where $\varphi = \varphi_{\mathrm{surf}} \exp(-11.8p)$ is the porosity, ϱ_{solid} and k_{solid} are the density and thermal conductivity of the compact solid material, respectively, and the pressure p is in GPa. For the seismic velocities, we calculate the bulk modulus based on that formula for the density of the porous material and the thermodynamic definition, $K = \varrho \partial p/\partial \varrho$, for physical consistency.

2 Rheological model

The viscosity η in our models is the same as in *Ruedas et al.* (2013b) and depends on temperature, pressure, melt, iron, and water content, and mineralogy. We used the general law for diffusion creep given by *Hirth and Kohlstedt* (2003, eq. 1), scaled with an additional factor to take into account the effect of an elevated iron content, after *Zhao et al.* (2009). The resulting formulation is therefore a function of pressure, temperature, porosity (in this case corresponding to the melt content) φ, Mg#, C_{OH}, and mineralogy X:

$$\begin{aligned}\eta(p,T,\varphi,\mathrm{Mg\#},C_{\mathrm{OH}},X) &= \eta_{\mathrm{p}}(X)\frac{b^3}{AC_{\mathrm{OH}}}\left(\frac{1-\mathrm{Mg\#_{ref}}}{1-\mathrm{Mg\#}}\right)^{1.5}\cdot \\ &\quad \exp\left[\frac{E+pV+c(\mathrm{Mg\#_{ref}}-\mathrm{Mg\#})}{RT}-a\varphi\right];\end{aligned} \tag{30}$$

in the dry case, C_{OH} is dropped from the formula, and the parameters for dry material are used. In practice, η is calculated for both the dry and the wet case, and the smaller value is used; this corresponds to a transition from wet to dry material if the concentration drops below a few ppm water.

We base the rheology on the model of a load-bearing framework, which means that the rheological properties of the volumetrically dominant mineral phase govern the behavior of the whole rock. In a peridotite, this would be olivine, and hence, it is the water concentration in olivine as determined via the partition coefficients (see Section 3) rather than the bulk

water concentration that is to be used for C_{OH}. For the reference case of a lherzolitic upper-mantle mineralogy, we used the values for dry or wet olivine ($A = 1.5 \cdot 10^9$ or 10^6, $E = 375$ or 335 kJ/mol, $V = 6 \cdot 10^{-6}$ or $4 \cdot 10^{-6}$ m^3/mol, respectively, and $a = 30$, *Hirth and Kohlstedt*, 2003); for this reference case, the petrological term $\eta_{\mathrm{p}}(X)$ is 1. Grain size b was fixed at 1 cm, and $\mathrm{Mg\#_{ref}}$ is 0.9. Deviations from this reference rheology due to the presence of basalt or eclogite or the transition to high-pressure polymorphs were treated by calculating volume-weighted averages with petrological factors of 2.5 (high-p polymorphs of the lower mantle layer, after *Jin et al.*, 2001), 0.25 (basalt, after *Mackwell et al.*, 1998), or 1.2 (eclogite, after *Jin et al.*, 2001), respectively.

3 Partition and exchange coefficients

The partition coefficient describes how a trace component X is distributed between two phases a and b:

$$D_{\mathrm{X}}^{\mathrm{a/b}} = \frac{C_{\mathrm{X}}^{\mathrm{a}}}{C_{\mathrm{X}}^{\mathrm{b}}}, \tag{31}$$

where C is the concentration (usually mass fraction); in many cases of interest, phase b is silicate melt. In reality, D is a function of p, T, and the composition of the solid phases and the melt, but often the available data are too scarce to provide robust information on these dependencies. This problem is particularly pressing in the case of most high-p minerals, for which there seem to be hardly any melt partitioning experiments. However, mineral–mineral partitioning information is available more frequently, and if mineral–melt partitioning is known for one mineral a, D for another mineral b may be estimated by

$$\frac{\frac{C_{\mathrm{X}}^{\mathrm{a}}}{C_{\mathrm{X}}^{\mathrm{liq}}}}{\frac{C_{\mathrm{X}}^{\mathrm{b}}}{C_{\mathrm{X}}^{\mathrm{liq}}}} = \frac{C_{\mathrm{X}}^{\mathrm{a}}}{C_{\mathrm{X}}^{\mathrm{b}}} = D_{\mathrm{X}}^{\mathrm{a/b}} = \frac{D_{\mathrm{X}}^{\mathrm{a/liq}}}{D_{\mathrm{X}}^{\mathrm{b/liq}}}. \tag{32}$$

This equation also enables us to calculate how a component is distributed between various mineral phases, if the mineral–melt partition coefficients are known; this is useful especially in the case of water, where the unequal distribution between the different mineral phases affects the physical properties, e.g., the viscosity, of the bulk mixture of the mineral constituents.

Apart from these relations for a single component and one or more minerals, it can also be useful to consider the partitioning, or exchange, of two components X and Y between two phases a and b. This exchange coefficient is the ratio of the respective partition coefficients,

$$\mathcal{K}_{\mathrm{X/Y}}^{\mathrm{a/b}} = \frac{D_{\mathrm{X}}^{\mathrm{a/b}}}{D_{\mathrm{Y}}^{\mathrm{a/b}}} = \frac{D_{\mathrm{X}}^{*\mathrm{a/b}}}{D_{\mathrm{Y}}^{*\mathrm{a/b}}}, \tag{33}$$

where phase b is often melt; the partition coefficients may be either mass or molar (marked with an asterisk) thanks to canceling terms (*Jones*, 1995). $\mathcal{K}$ tends to be less sensitive to T and composition, and we use it in some cases for calculating the change in Mg# upon melting.

In the following, we give a brief overview of the parameterizations we used for minerals in our models. In some cases, it has been possible to put them on a physical foundation such as lattice-strain theory, but often only a simple phenomenological description is possible; it is hoped that these parameterizations will continually be improved and that formulations

more suitable for use in geodynamical models will become more common in the geochemical literature. The main purpose of the parameterizations here is to capture the general trends in the variability of the partition coefficients with p, T, and composition and thus improve upon models that assume constant coefficients, but the formulae given below, unless they are cited from the geochemical literature, may not always be accurate enough for use in detailed geochemical models. They are intended for use in our geodynamical model that can only include chemistry at a very primitive level.

Unless mentioned otherwise, pressures are given in GPa and temperatures are given in K. In several cases, compositional information for the mineral phases under consideration is needed; generally, the basis for deriving estimated values for use in those formulae is the silicate bulk composition of the mantle and crust of the planet.

Olivine $\mathcal{K}_{\mathrm{Fe/Mg}}^{\mathrm{ol/liq}}$ can be expressed in terms of p, T, the molar silica content of the melt $\bar{X}_{\mathrm{SiO_2}}$, and the Mg# of the olivine as

$$\mathcal{K}_{\mathrm{Fe/Mg}}^{\mathrm{ol/liq}} = (3.6\bar{X}_{\mathrm{SiO_2}} - 0.22)\exp\left(\frac{350p - 7.34T - 3766.035 - 6000\mathrm{Mg\#}}{RT}\right) \tag{34}$$

(rewritten from *Toplis*, 2005, eq. 10), where we determine $\bar{X}_{\mathrm{SiO_2}}$ from the bulk composition of the crust if possible.

Taura et al. (1998) measured partitioning between olivine and melt for various elements including K at T between 1873 and 2273 K and p between 3 and 15 GPa. Leaving out the probably spurious point for KLB-28, their data can be fitted by

$$D_{\mathrm{K}}^{\mathrm{ol/liq}} = \exp\left(5.16279p + \frac{-10933.9p + 51567.8 - 28.3621T}{T}\right). \tag{35}$$

For $T \lesssim 1750$ K and low p, this fit will quickly become unreliable, and extrapolation at the high-p,T end is not recommended either; we use the values at the experimental bounds for p,T outside this range and cap $D_{\mathrm{K}}^{\mathrm{ol/liq}}$ at 0.1, close to the highest value from *Taura et al.* (1998) deemed reliable.

For Th^{4+} and U^{4+} there are not enough data to establish a quantitative model; we use a value of $D_{\mathrm{U}}^{\mathrm{ol/liq}} = 6 \times 10^{-5}$ and the ratio $D_{\mathrm{U}}^{\mathrm{ol/liq}}/D_{\mathrm{Th}}^{\mathrm{ol/liq}} = 6.3$ recommended by *Blundy and Wood* (2003, Tab. 6).

The partition coefficient for water was derived by fitting the ratio of Arrhenius-type solubility laws to experimental data from *Koga et al.* (2003), *Aubaud et al.* (2004), *Hauri et al.* (2006), *Tenner et al.* (2009), *O'Leary et al.* (2010), *Novella et al.* (2014), and the high-p set from *Tenner et al.* (2012) and found

$$D_{\mathrm{H_2O}}^{\mathrm{ol/liq}}(p, T, C_{\mathrm{H_2O}}^{\mathrm{ol}}) = 0.115\sqrt{C_{\mathrm{H_2O}}^{\mathrm{ol}}}\exp\left(\frac{259.0635 + 108.249p}{T}\right). \tag{36}$$

Orthopyroxene We determined $D_{\mathrm{MgO}}^{*\mathrm{ol/liq}}$ according to the formulae in the previous section and eq. 33 and use the result in the relation

$$D_{\mathrm{FeO}}^{*\mathrm{ol/liq}} = 0.129D_{\mathrm{MgO}}^{*\mathrm{ol/liq}} + 0.264 \tag{37}$$

(*Jones*, 1995).

For K, we use a constant value of $D_{\mathrm{K}}^{\mathrm{opx/liq}} = 4.85 \times 10^{-3}$ (*van Kan Parker et al.*, 2010). Th^{4+} and U^{4+} partitioning studies are limited to basaltic compositions and indicate that $D_{\mathrm{U}}^{\mathrm{opx/liq}} \geq D_{\mathrm{Th}}^{\mathrm{opx/liq}}$, with a best estimate of $D_{\mathrm{U}}^{\mathrm{opx/liq}}/D_{\mathrm{Th}}^{\mathrm{opx/liq}} \approx 2.52$ (*Blundy and Wood*, 2003; *Wood and Blundy*, 2014).

Partitioning of water essentially follows *O'Leary et al.* (2010, eqs. 12, A8, A9), who parameterize it as

$$D_{\mathrm{H_2O}}^{\mathrm{opx/liq}} = \exp\left(-5.66 + 8.4\hat{X}_{\mathrm{Al}}^{\mathrm{opx}} + 10\hat{X}_{\mathrm{Ca}}^{\mathrm{opx}}\right), \tag{38}$$

where the atomic fraction of Al^{3+} on the M1 site of opx, $\hat{X}_{\mathrm{Al}}^{\mathrm{opx}}$, is determined from

$$\hat{X}_{\mathrm{Al}}^{\mathrm{opx}} = \begin{cases} 0.032 + 0.056p, & p \leq 2.83\,\mathrm{GPa} \\ \max(0, 0.4 - 0.2\ln p), & \text{else.} \end{cases} \tag{39}$$

In their parameterization, $\hat{X}_{\mathrm{Ca}}^{\mathrm{opx}}$ has the constant value 0.074 atoms per formula unit, whereas we solve the Ca-in-opx thermometer from *Brey and Köhler* (1990) for it:

$$\hat{X}_{\mathrm{Ca}}^{\mathrm{opx}} = \exp\left(-\frac{6425 + 264p}{T} + 1.843\right). \tag{40}$$

Clinopyroxene From parameterizations of the partition coefficient for MgO and FeO from *Langmuir et al.* (1992, tab. C1), we estimate $D_{\mathrm{Fe}}^{*\mathrm{cpx/liq}}/D_{\mathrm{Mg}}^{*\mathrm{cpx/liq}} \approx 0.24$.

For K, we constructed a model formula of the form used for partitioning of Na by *Blundy et al.* (1995) and fitted it to experimental data (*Harlow*, 1997; *Hauri et al.*, 1994; *Chamorro et al.*, 2002; *Brooker et al.*, 2003; *Dygert et al.*, 2014):

$$D_{\mathrm{K}}^{\mathrm{cpx/liq}}(p,T) = \exp\left(\frac{-6738.9 + 1974.2p + 110.35p^2}{T} - 1.6249 - 0.88006p - 0.064808p^2\right); \tag{41}$$

this fit seems to work best for $p \lesssim 8\,\mathrm{GPa}$ but should not be considered better than an order-of-magnitude approximation.

For $D_{\mathrm{Th}}^{\mathrm{cpx/liq}}$, we use the p–T parameterization by *Landwehr et al.* (2001) and derive $D_{\mathrm{U}}^{\mathrm{cpx/liq}}$ from the result using lattice-strain theory, applying a relation for the partition coefficients of ions of different radius but same valence (4+ in this case) (*Wood and Blundy*, 2014, section 3.11.2). For details, the reader is referred to those papers.

The partitioning of water is calculated again according to the formulae given by *O'Leary et al.* (2010, modified after eqs. 11, A5–A7):

$$D_{\mathrm{H_2O}}^{\mathrm{cpx-liq}} = \exp\left(-5 + 6.3\hat{X}_{\mathrm{T\,Al}}^{\mathrm{cpx}} - 1.2\hat{X}_{\mathrm{Ca}}^{\mathrm{cpx}} + \frac{1600}{T}\right), \tag{42}$$

where the atomic fraction of Al on the tetrahedral site in clinopyroxene is

$$\hat{X}_{\mathrm{T\,Al}}^{\mathrm{cpx}} = \begin{cases} 0.067 + 0.03p, & p \leq 2.6\,\mathrm{GPa} \\ \max(0, 0.26 - 0.12\ln p), & \text{else} \end{cases} \tag{43}$$

and the Ca fraction on the M2 site is

$$\hat{X}_{\mathrm{Ca}}^{\mathrm{cpx}} = \min[\max(0, 0.7 - 0.23\ln p), 1 - \hat{X}_{\mathrm{Na}}^{\mathrm{cpx}}]. \tag{44}$$

Garnet The starting point for the partitioning of Th, U as well as Fe is again lattice-strain theory. *van Westrenen et al.* (2001) and *Wood and Blundy* (2002) have developed a detailed parameterization for trivalent cations that also includes a parameterization for $D_{\mathrm{Mg}}^{\mathrm{gt/liq}}$. The latter can be combined with a formula for the cpx–gt exchange coefficient of Mg and Fe,

$$\mathcal{K}_{\mathrm{Fe/Mg}}^{\mathrm{gt/liq}} = 0.24 \exp\left(2.33 - \frac{3686 + 283.5p}{T}\right) \tag{45}$$

(*Råheim and Green*, 1974), and eq. 33 to determine the partitioning of Fe. Partitioning of (tetravalent) Th and U extrapolates from the parameterization for trivalent ions following *Wood and Blundy* (2014, eq. 29) with $\epsilon = 12$ for Mg-rich, Fe,Ca-bearing aluminous garnet (*Shannon*, 1993) and the ionic radii from *Wood et al.* (1999) for Th^{4+} and U^{4+}; for details, the reader is referred to the original papers, especially the comprehensive review by *Wood and Blundy* (2014), which has been our guide in many respects.

The few data for water do not show a clear trend and are insufficient to derive a p,T-dependent formulation, so we a constant value of 0.0026 from averaging various experimental data (*Hauri et al.*, 2006; *Aubaud et al.*, 2008; *Tenner et al.*, 2009; *Novella et al.*, 2014).

Wadsleyite Experimental data for high-p minerals are scarce. $\mathcal{K}_{\mathrm{Fe/Mg}}^{\mathrm{wd/liq}}$ may vary substantially with p and T, but T for the two data points listed by *Jones* (1995) differs by only 60 K, and so we assumed that the variation is mostly due to p:

$$\mathcal{K}_{\mathrm{Fe/Mg}}^{\mathrm{wd/liq}} = \max(1.25, 5.304 - 0.2457p). \tag{46}$$

For Th and U, we take the values 0.013 and 1.5×10^{-5}, respectively, from *Mibe et al.* (2006), and for water, we multiply the partition coefficient for olivine at 13.1 GPa with $D_{\mathrm{H_2O}}^{\mathrm{wd/ol}} = 4.95$ (*Chen et al.*, 2002) to determine at least a constant estimate for $D_{\mathrm{H_2O}}^{\mathrm{wd/liq}}$.

Ringwoodite We know of no data for $\mathcal{K}_{\mathrm{Fe/Mg}}^{\mathrm{rw/liq}}$, so we assume that the structural similarity with wadsleyite results in a similar partitioning behavior and use a constant value of 0.39, which is the higher-p value given by *Jones* (1995).

Some data exist for a limited p range for water–melt partitioning in iron-free ringwoodite. They indicate a twofold increase of $D_{\mathrm{H_2O}}^{\mathrm{rw/liq}}$ from 20 to 23 GPa, but a clear T dependence cannot be deduced (*Ohtani et al.*, 2000). We fitted these data with

$$D_{\mathrm{H_2O}}^{\mathrm{rw/liq}} = 5.75 \times 10^{-3} p - 0.09125, \tag{47}$$

which should be satisfactory, given the scarce data, because extrapolation far outside the p range from 20 to 23 GPa will not be necessary, given the narrow stability field of the mineral.

Majorite *Jones* (1995) has compiled some $\mathcal{K}_{\mathrm{Fe/Mg}}^{\mathrm{mj/liq}}$ data for majorite from different sources. There is no clear p trend but some indication for a decrease of $\mathcal{K}_{\mathrm{Fe/Mg}}^{\mathrm{mj/liq}}$ with increasing T. We fitted these data with

$$\mathcal{K}_{\mathrm{Fe/Mg}}^{\mathrm{mj/liq}} = 1.126 - 3.14 \times 10^{-4} T, \tag{48}$$

but the trend for $D_{\mathrm{Fe}}^{\mathrm{mj/liq}}$ is even less clear, with data in the range 16–26 GPa/2173–2473 K scattering around ~ 0.35.

Corgne and Wood (2004) have measured partitioning between majorite and melt for K, Th, and U. The partitioning of water can be inferred in two steps: from $D_{\mathrm{H_2O}}^{\mathrm{rw/st}} \approx 521$ and $D_{\mathrm{H_2O}}^{\mathrm{mj/st}} \approx 270$ (*Bolfan-Casanova et al.*, 2000) follows $D_{\mathrm{H_2O}}^{\mathrm{rw/mj}} = 1.93$, and so the result for $D_{\mathrm{H_2O}}^{\mathrm{rw/liq}}$ in eq. 47, divided by 1.93, yields:

$$D_{\mathrm{H_2O}}^{\mathrm{mj/liq}} = 2.95 \times 10^{-3} p - 0.04679. \tag{49}$$

4 Description of supplementary datasets

The files in the following list can be retrieved from Figshare at `https://doi.org/10.6084/m9.figshare.c.3777686`.

`f.dat` Present-day depth–depletion profiles of Figure 7a of the main text. The first two data blocks contain global lateral averages of the Reference models Ref-36 (TC and T), the subsequent blocks contain local radial profiles taken at the impact sites of models H-36 (TC and T), I-36 (TC and T), U-36 (TC and T), I-72 (TC and T), and I-144 (TC and T); these local profiles are smoothed (downsampled by a factor of 3 or 4) for clarity when plotting. The columns contain depth z in m, pressure p in Pa, and the depletion variable f ($f > 0$: depleted, $f < 0$: enriched/basaltic).

`I-36-T_f.dat` Data of the depletion (f) snapshots of model I-36 (T) in the rightmost column of Figure 3 of the main paper. Each data block contains the data of one snapshot. The columns contain the lateral coordinate (ϕ) in degrees, the depth (z) in m, and the depletion.

`I-36-T_T.dat` Data of the temperature (T) snapshots of model I-36 (T) in the center-right column of Figure 3 of the main paper. Each data block contains the data of one snapshot. The columns contain the lateral coordinate (ϕ) in degrees, the depth (z) in m, and the temperature in K.

`I-36-TC_f.dat` Data of the depletion (f) snapshots of model I-36 (TC) in the center-left column of Figure 3 of the main paper. Each data block contains the data of one snapshot. The columns contain the lateral coordinate (ϕ) in degrees, the depth (z) in m, and the depletion.

`I-36-TC_T.dat` Data of the temperature (T) snapshots of model I-36 (TC) in the leftmost column of Figure 3 of the main paper. Each data block contains the data of one snapshot. The columns contain the lateral coordinate (ϕ) in degrees, the depth (z) in m, and the temperature in K.

`marssol.dat` Compilation of experimental values used in Appendix B and Figure A.1 of the main text. The columns contain the pressure in GPa, the temperature in °C, and (for informational purposes only) the extant phases if known.

`qs_t.dat` Time evolution of the surface heat flow q_s of the Reference, Huygens, and Utopia (impact at 400 My) model series for initial water contents of 36 and 144 ppm (TC and T). The columns contain time t in My and q_s in W/m^2.

`Raeff10_t.dat` Time evolution of 10 My-averages of the effective Rayleigh number of the Reference and Utopia (impact at 400 My) model series for initial water contents of 36, 72, and 144 ppm (TC and T) (Figure 2 of the main text); the values are centered on the middle of the averaging interval. The columns contain time t in My and the effective Rayleigh number. One spurious average value was masked.

`Ref-36-TC_T.dat` Data of the temperature (T) snapshot of model Ref-36 (TC) in the lower right quarter of Figure 4 of the main paper. The columns contain the lateral coordinate (ϕ) in degrees, the depth (z) in m, and the temperature in K.

`rho.dat` Present-day depth–density profiles of Figure 7b of the main text. The first two data blocks contain global lateral averages of the Reference models Ref-36 (TC and T), the subsequent blocks contain local radial profiles taken at the impact sites of models H-36 (TC and T), I-36 (TC and T), U-36 (TC and T), I-72 (TC and T), and I-144 (TC and T). The columns contain depth z in m, pressure p in Pa, and density ϱ in kg/m^3. The very last data block contains the experimental data from *Bertka and Fei* (1998) as retrieved from their Fig. 1, with p in GPa and ϱ in kg/m^3.

`U-36-T_T.dat` Data of the temperature (T) snapshot of model U-36 (T) in the lower left quarter of Figure 4 of the main paper. The columns contain the lateral coordinate (ϕ) in degrees, the depth (z) in m, and the temperature in K.

`U-36-TC_T.dat` Data of the temperature (T) snapshots of model U-36 (TC) in the upper row of Figure 4 of the main paper. Each data block contains the data of one snapshot. The columns contain the lateral coordinate (ϕ) in degrees, the depth (z) in m, and the temperature in K.

`vB.dat` Present-day depth–bulk sound velocity profiles of Figure 8 of the main text. The first data block contains global lateral averages of the Reference models Ref-36 (TC), the subsequent blocks contain local radial profiles taken at the impact sites of the TC variants of models H-36, I-36, U-36, I-72, and I-144. The columns contain depth z in m, pressure p in Pa, density ϱ in kg/m^3, and the Voigt–Reuss–Hill average of the adiabatic bulk modulus K_S in Pa; the bulk sound velocity can then be calculated as $v_\mathrm{B} = \sqrt{K_S/\varrho}$.

`zle_t.dat` Time evolution of the elastic thickness of the lithosphere z_el of the Reference, Huygens, and Utopia (impact at 400 My) model series for initial water contents of 36 and 144 ppm (TC and T). For data blocks 1–12, the columns contain time t in My and z_el in km. The data blocks from 13 onward contain minimum and maximum estimates for the ages in Ma, for q_s in mW/m^2 (for informational purposes only, unused here), and for z_el in km. The ages used for plotting are the arithmetic means of the minimum and maximum ages. For z_el, the arithmetic mean of the minimum and maximum was used where available, otherwise only the minimum value was given; the errorbars in the plot indicate the minimum and maximum values. Absence of data is indicated by a dot.

`I-36_TC.mp4` Animation of the temporal evolution of temperature and composition (depletion) in model I-36/TC. Snapshots from this animation are shown in the left panel of Figure 3 of the main paper.

`I-36_T.mp4` Animation of the temporal evolution of temperature and composition (depletion) in model I-36/T. Snapshots from this animation are shown in the right panel of Figure 3 of the main paper.

References

Abramowitz, M., and I. A. Stegun (Eds.), *Handbook of Mathematical Functions*, U.S. National Bureau of Standards, 1964.

Ashcroft, N. W., and N. D. Mermin, *Solid State Physics*, Saunders College Publishing, 1976.

Aubaud, C., E. H. Hauri, and M. M. Hirschmann, Hydrogen partition coefficients between nominally anhydrous minerals and basaltic melts, *Geophys. Res. Lett.*, *31*, L20611, doi: 10.1029/2004GL021341, 2004.

Aubaud, C., M. M. Hirschmann, A. C. Withers, and R. L. Hervig, Hydrogen partitioning between melt, clinopyroxene, and garnet at 3 GPa in a hydrous MORB with 6 wt.% H_2O, *Contrib. Mineral. Petrol.*, *156*(5), 607–625, doi:10.1007/s00410-008-0304-2, 2008.

Berryman, J. G., Mixture theories for rock properties, in *Rock Physics & Phase Relations — A Handbook of Physical Constants*, *AGU Reference Shelf*, vol. 3, edited by T. J. Ahrens, pp. 205–228, American Geophysical Union, Washington, D.C., 1995.

Bertka, C. M., and Y. Fei, Density profile of an SNC model Martian interior and the moment-of-inertia factor of Mars, *Earth Planet. Sci. Lett.*, *157*(1–2), 79–88, doi:10.1016/S0012-821X(98)00030-2, 1998.

Blundy, J., and B. Wood, Mineral–melt partitioning of uranium, thorium and their daughters, in *Uranium-series Geochemistry*, edited by B. Bourdon, G. M. Henderson, C. C. Lundstrom, and S. P. Turner, no. 52 in Rev. Mineral. Geochem., pp. 59–123, Mineralogical Society of America, Washington, D.C., 2003.

Blundy, J. D., T. J. Falloon, B. J. Wood, and J. A. Dalton, Sodium partitioning between clinopyroxene and silicate melts, *J. Geophys. Res.*, *100*(B8), 15,501–15,515, 1995.

Bolfan-Casanova, N., H. Keppler, and D. C. Rubie, Water partitioning between nominally anhydrous minerals in the MgO–SiO_2–H_2O system up to 24 GPa: implications for the distribution of water in the Earth's mantle, *Earth Planet. Sci. Lett.*, *182*, 209–221, 2000.

Brey, G. P., and T. Köhler, Geothermobarometry in four-phase lherzolites II. New thermobarometers, and practical assessment of existing thermobarometers, *J. Petrol.*, *31*(6), 1353–1378, doi:10.1093/petrology/31.6.1353, 1990.

Brooker, R. A., Z. Du, J. D. Blundy, S. P. Kelley, N. L. Allan, B. J. Wood, E. M. Chamorro, J.-A. Wartho, and J. A. Purton, The 'zero charge' partitioning behaviour of noble gases during mantle melting, *Nature*, *423*, 738–741, doi:10.1038/nature01708, 2003.

Chamorro, E. M., R. A. Brooker, J.-A. Wartho, B. J. Wood, S. P. Kelley, and J. D. Blundy, Ar and k partitioning between clinopyroxene and silicate melt to 8 gpa, *Geochim. Cosmochim. Acta*, *66*(3), 507–519, 2002.

Chen, J., T. Inoue, H. Yurimoto, and D. Weidner, Effect of water on olivine–wadsleyite phase boundary in the $(Mg, Fe)_2SiO_4$ system, *Geophys. Res. Lett.*, *29*(18), 22, 2002.

Corgne, A., and B. J. Wood, Trace element partitioning between majoritic garnet and silicate melt at 25 GPa, *Phys. Earth Planet. Inter.*, *143–144*, 407–419, doi:10.1016/j.pepi.2003.08.012, 2004.

Debye, P., Zur Theorie der spezifischen Wärme, *Ann. Phys.*, *IV/39*, 789–839, 1912.

Duffy, T. S., and D. L. Anderson, Seismic velocities in mantle minerals and the mineralogy of the upper mantle, *J. Geophys. Res.*, *94*(B2), 1895–1912, 1989.

Dygert, N., Y. Liang, C. Sun, and P. Hess, An experimental study of trace element partitioning between augite and Fe-rich basalts, *Geochim. Cosmochim. Acta*, *132*, 170–186, doi:10.1016/j.gca.2014.01.042,10.1016/j.gca.2014.09.013, corrigendum in 149, 281–283, 2014.

Fornberg, B., Calculation of weights in finite difference formulas, *SIAM Rev.*, *40*(3), 685–691, 1998.

Grüneisen, E., Theorie des festen Zustandes einatomiger Elemente, *Ann. Phys.*, *39*, 257–306, 1912.

Grüneisen, E., Zustand des festen körpers, in *Thermische Eigenschaften der Stoffe*, *Handbuch der Physik*, vol. 10, edited by C. Drucker, E. Grüneisen, P. Kohnstamm, F. Körber, K. Scheel, E. Schrödinger, F. Simon, J. D. van der Waals, Jr., and F. Henning, chap. 1, pp. 1–59, Springer, Heidelberg, 1926.

Harlow, G. E., K in clinopyroxene at high pressure and temperature: An experimental study, *Amer. Mineral.*, *82*(3–4), 259–269, 1997.

Hauri, E. H., T. P. Wagner, and T. L. Grove, Experimental and natural partitioning of Th, U, Pb and other trace elements between garnet, clinopyroxene and basaltic melts, *Chem. Geol.*, *117*, 149–166, 1994.

Hauri, E. H., G. A. Gaetani, and T. H. Green, Partitioning of water during melting of the Earth's upper mantle at H_2O-undersaturated conditions, *Earth Planet. Sci. Lett.*, *248*(3–4), 715–734, 2006.

Head, J. W., and L. Wilson, Magma reservoirs and neutral buoyancy zones on Venus: Implications for the formation and evolution of volcanic landforms, *J. Geophys. Res.*, *97*(E3), 3877–3903, doi:10.1029/92JE00053, 1992.

Hirth, G., and D. L. Kohlstedt, Rheology of the upper mantle and the mantle wedge: A view from the experimentalists, in *Inside the Subduction Factory*, *AGU Geophysical Monograph*, vol. 138, edited by J. Eiler, pp. 83–105, American Geophysical Union, Washington, D.C., 2003.

Hofmeister, A. M., Mantle values of thermal conductivity and the geotherm from phonon lifetimes, *Science*, *283*, 1699–1706, 1999.

Hofmeister, A. M., and J. M. Branlund, Thermal conductivity of the earth, in *Mineral Physics*, *Treatise on Geophysics*, vol. 2, edited by G. D. Price and L. Stixrude, 2nd ed., chap. 2.23, pp. 583–608, Elsevier, doi:10.1016/B978-0-444-53802-4.00047-6, 2015.

Ita, J., and L. Stixrude, Petrology, elasticity, and composition of the mantle transition zone, *J. Geophys. Res.*, *97*(B5), 6849–6866, 1992.

Jin, Z.-M., J. Zhang, H. W. Green, II, and S. Jin, Eclogite rheology: Implications for subducted lithosphere, *Geology*, *29*(8), 667–670, 2001.

Jones, J. H., Experimental trace element partitioning, in *Rock Physics and Phase Relations — A Handbook of Physical Constants*, *AGU Reference Shelf*, vol. 3, edited by T. J. Ahrens, pp. 73–104, American Geophysical Union, Washington, D.C., 1995.

Koga, K., E. Hauri, M. M. Hirschmann, and D. Bell, Hydrogen concentration analyses using SIMS and FTIR: Comparison and calibration for nominally anhydrous minerals, *Geochem. Geophys. Geosyst.*, *4*(2), doi:10.1029/2002GC000378, 2003.

Landwehr, D., J. Blundy, E. M. Chamorro-Perez, E. Hill, and B. Wood, U-series disequilibria generated by partial melting of spinel lherzolite, *Earth Planet. Sci. Lett.*, *188*(3–4), 329–348, doi:10.1016/S0012-821X(01)00328-4, 2001.

Langmuir, C. H., E. M. Klein, and T. Plank, Petrological systematics of mid-ocean ridge basalts: Constraints on melt generation beneath ocean ridges, in *Mantle Flow and Melt Generation at Mid-Ocean Ridges*, edited by J. Phipps Morgan, D. K. Blackman, and J. M. Sinton, no. 71 in Geophysical Monographs, pp. 183–280, American Geophysical Union, Washington, D.C., doi:10.1029/GM071p0183, 1992.

Leone, G., L. Wilson, and A. G. Davies, The geothermal gradient of Io: Consequences for lithosphere structure and volcanic eruptive activity, *Icarus*, *211*(1), 623–635, doi:10.1016/j.icarus.2010.10.016, 2011.

Mackwell, S. J., M. E. Zimmerman, and D. L. Kohlstedt, High-temperature deformation of dry diabase with application to tectonics on Venus, *J. Geophys. Res.*, *103*(B1), 975–984, 1998.

Mamedov, B. A., E. Eser, H. Koç, and I. M. Askerov, Accurate evaluation of the specific heat capacity of solids and its application to MgO and ZnO crystals, *Int. J. Thermophys.*, *30*(3), 1048–1054, 2009.

Mibe, K., Y. Orihashi, S. Nakai, and T. Fujii, Element partitioning between transition-zone minerals and ultramafic melt under hydrous conditions, *Geophys. Res. Lett.*, *33*, L16307, doi:10.1029/2006GL026999, 2006.

Novella, D., D. J. Frost, E. H. Hauri, H. Bureau, C. Raepsaet, and M. Roberge, The distribution of H_2O between silicate melt and nominally anhydrous peridotite and the onset of hydrous melting in the deep upper mantle, *Earth Planet. Sci. Lett.*, *400*, 1–13, doi:10.1016/j.epsl.2014.05.006, 2014.

Ohtani, E., H. Mizobata, and H. Yurimoto, Stability of dense hydrous magnesium silicate phases in the systems Mg_2SiO_4–H_2O and $MgSiO_3$–H_2O at pressures up to 27 GPa, *Phys. Chem. Min.*, *27*(8), 533–544, doi:10.1007/s002690000097, 2000.

O'Leary, J. A., G. A. Gaetani, and E. H. Hauri, The effect of tetrahedral Al^{3+} on the partitioning of water between clinopyroxene and silicate melt, *Earth Planet. Sci. Lett.*, *297*(1–2), 111–120, 2010.

Poirier, J.-P., *Introduction to the Physics of the Earth's Interior*, 2 ed., Cambridge University Press, 2000.

Råheim, A., and D. H. Green, Experimental determination of the temperature and pressure dependence of the Fe-Mg partition coefficient for coexisting garnet and clinopyroxene, *Contrib. Mineral. Petrol.*, *48*(3), 179–203, 1974.

Robie, R. A., and B. S. Hemingway, Thermodynamic properties of minerals and related substances at 298.15 k and 1 bar (10^5 pascals) pressure and at higher temperatures, *U.S. Geological Survey Bulletin 2131*, U.S. Geological Survey, Washington, D.C., 1995.

Robie, R. A., B. S. Hemingway, and J. R. Fisher, Thermodynamic properties of minerals and related substances at 298.15 k and 1 bar (10^5 pascals) pressure and at higher temperatures, *U.S. Geological Survey Bulletin 1452*, U.S. Geological Survey, Washington, D.C., reprinted with corrections 1979, 1978.

Ruedas, T., P. J. Tackley, and S. C. Solomon, Thermal and compositional evolution of the martian mantle: Effects of phase transitions and melting, *Phys. Earth Planet. Inter.*, *216*, 32–58, doi:10.1016/j.pepi.2012.12.002, 2013a.

Ruedas, T., P. J. Tackley, and S. C. Solomon, Thermal and compositional evolution of the martian mantle: Effect of water, *Phys. Earth Planet. Inter.*, *220*, 50–72, doi:10.1016/j.pepi.2013.04.006, 2013b.

Shannon, R. D., Dielectric polarizabilities of ions in oxides and fluorides, *J. Appl. Phys.*, *73*(1), 348–366, doi:10.1063/1.353856, 1993.

Stacey, F. D., Thermoelasticity of a mineral composite and a reconsideration of lower mantle properties, *Phys. Earth Planet. Inter.*, *106*, 219–236, 1998.

Stacey, F. D., and P. M. Davis, High pressure equations of state with applications to the lower mantle and core, *Phys. Earth Planet. Inter.*, *142*(3–4), 137–184, doi:10.1016/j.pepi.2004.02.003, 2004.

Stixrude, L., and M. S. T. Bukowinski, Fundamental thermodynamic relations and silicate melting with implications for the constitution of D″, *J. Geophys. Res.*, *95*(B12), 19,311–19,325, 1990.

Taura, H., H. Yurimoto, K. Kurita, and S. Sueno, Pressure dependence on partition coefficients for trace elements between olivine and the coexisting melts, *Phys. Chem. Min.*, *25*(7), 469–484, doi:10.1007/s002690050138, 1998.

Tenner, T. J., M. M. Hirschmann, A. C. Withers, and R. L. Hervig, Hydrogen partitioning between nominally anhydrous upper mantle minerals and melt between 3 and 5 GPa and applications to hydrous peridotite partial melting, *Chem. Geol.*, *262*(1–2), 42–56, 2009.

Tenner, T. J., M. M. Hirschmann, A. C. Withers, and P. Ardia, H_2O storage capacity of olivine and low-Ca pyroxene from 10 to 13 GPa: consequences for dehydration melting above the transition zone, *Contrib. Mineral. Petrol.*, *163*(2), 297–316, doi:10.1007/s00410-011-0675-7, erratum in *Contrib. Mineral. Petrol.* 163(2), p. 317–318, doi:10.1007/s00410-011-0684-6, 2012.

Toplis, M. J., The thermodynamics of iron and magnesium partitioning between olivine and liquid: criteria for assessing and predicting equilibrium in natural and experimental systems, *Contrib. Mineral. Petrol.*, *149*(1), 22–39, 2005.

van Kan Parker, M., A. Liebscher, D. Frei, J. van Sijl, W. van Westrenen, J. Blundy, and G. Franz, Experimental and computational study of trace element distribution between orthopyroxene and anhydrous silicate melt: substitution mechanisms and the effect of iron, *Contrib. Mineral. Petrol.*, *159*(4), 459–473, doi:10.1007/s00410-009-0435-0, 2010.

van Westrenen, W., J. D. Blundy, and B. J. Wood, High field strength element/rare earth element fractionation during partial melting in the presence of garnet: Implications for identification of mantle heterogeneities, *Geochem. Geophys. Geosyst.*, *2*(7), 1039, doi: 10.1029/2000GC000133, 2001.

Wood, B. J., and J. D. Blundy, The effect of H_2O on crystal–melt partitioning of trace elements, *Geochim. Cosmochim. Acta*, *66*(20), 3647–3656, 2002.

Wood, B. J., and J. D. Blundy, Trace element partitioning: The influences of ionic radius, cation charge, pressure, and temperature, in *The Mantle and Core*, *Treatise on Geochemistry*, vol. 3, edited by R. W. Carlson, 2nd ed., chap. 3.11, pp. 421–448, Elsevier, doi:10.1016/B978-0-08-095975-7.00209-6, 2014.

Wood, B. J., J. D. Blundy, and J. A. C. Robinson, The role of clinopyroxene in generating U-series disequilibrium during mantle melting, *Geochim. Cosmochim. Acta*, *63*(10), 1613–1620, 1999.

Zhao, Y., M. E. Zimmerman, and D. L. Kohlstedt, Effect of iron content on the creep behavior of olivine: 1. Anhydrous conditions, *Earth Planet. Sci. Lett.*, *287*(1–2), 229–240, doi:10.1016/j.epsl.2009.08.006, 2009.